

Chapter 4

Control of Intrinsic Point Defects in Single-Crystal Si and Ge Growth from a Melt

Jan Vanhellemont, Kozo Nakamura, Eiji Kamiyama, and Koji Sueoka

Abstract The so called Voronkov criterion defines a critical value Γ_{crit} of the ratio $\Gamma = v/G$ of the pulling rate v over the thermal gradient G at the crystal-melt/interface of a growing crystal. For $\Gamma > \Gamma_{crit}$, the crystal is vacancy-rich and can contain large vacancy clusters that are detrimental for gate oxide performance and for thin film epitaxial growth. For $\Gamma < \Gamma_{crit}$, the crystal is self-interstitial-rich and in the worst case will contain dislocation clusters. For $\Gamma \approx \Gamma_{crit}$, the crystal is free of grown-in intrinsic point defect clusters and optimal for device processing. Analytical expressions have been derived describing Γ_{crit} as function of intrinsic point defect parameters. The impact of thermal stress σ_{th} at the crystal-melt interface and of crystal doping on Γ_{crit} will be clarified. As σ_{th} increases with increasing crystal diameter, controlling G and v will become a real challenge for the development of future 450 mm diameter, defect free Si crystals. The possible application of the Voronkov criterion for Ge single-crystal growth from a melt will also briefly be discussed. Besides the impact of stress on intrinsic point defect formation energies and diffusivities, DFT calculations also suggest that near the crystal-melt interface, assumed to be stress free, the formation energy of the intrinsic point defects is lower than in the bulk of the crystal. This leads to thermal equilibrium concentrations of intrinsic point defects at the crystal-melt interface that are considerably different from those in the bulk which should be taken into account when applying the Voronkov criterion and also for intrinsic defect engineering in general. The Voronkov criterion was established for a flat interface. During crystal growth the crystal-melt interface is however curved which will have a significant impact on the diffusion of the intrinsic point defects. The impact of this curvature is discussed in detail both theoretically and experimentally.

J. Vanhellemont (✉)

Department of Solid State Sciences, Ghent University, Krijgslaan 281-S1, Gent B-9000, Belgium
e-mail: jan.vanhellemont@ugent.be

K. Nakamura • E. Kamiyama • K. Sueoka

Department of Communication Engineering, Okayama Prefectural University, 111 Kuboki, Soja, Okayama 719-1197, Japan
e-mail: kozo_nakamura@nifty.ne.jp; ejkamiyama@aol.com; sueoka@c.oka-pu.ac.jp

Keywords Silicon • Germanium • Single crystal pulling • Intrinsic point defect • Grown-in defect • Doping effect • Stress effect • Fermi-level effect

4.1 Introduction: A Very Brief History of Si and Ge Crystal Pulling

The first Si single-crystals were pulled in the early 1950s and had a diameter of about 10 mm and a weight of the order of 100 g [91]. Driven mainly by the expected cost reduction of fabricated devices, since that time, the silicon wafer diameter and thus also the diameter of Si crystals grown by the Czochralski (CZ) technique increased in steps with standard wafer diameters of 50, 75, 100, 125, 150, 200 and then to reach in one step the 300 mm by the end of the 1990s with crystal weights of about 300 kg as shown in Figs. 4.1 and 4.2.

By the end of the 1990s, The Japanese government also initiated the Super Silicon (SSi) project which was aiming at a feasibility study of 400 mm crystal growth [58]. The obtained results indicated that it was possible to grow vacancy-rich and interstitial-rich 400 mm crystals and that therefore it should also be possible to grow so called perfect Si 400 mm crystals, not containing large intrinsic point defect clusters and therefore suitable for advanced device mass production. At this

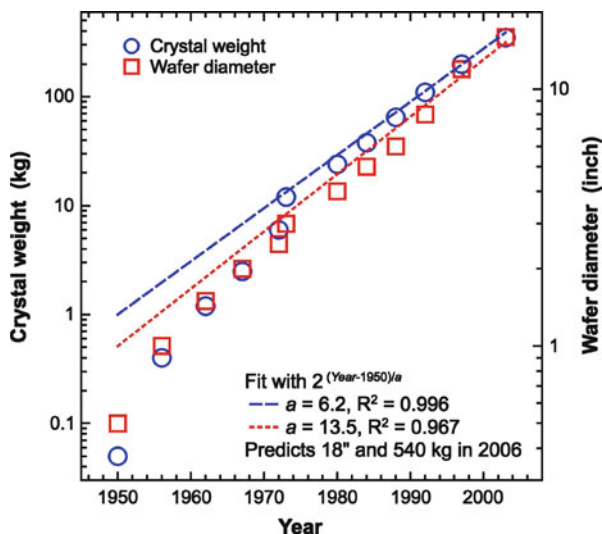


Fig. 4.1 Evolution of CZ Si wafer diameter and crystal weight with time [91]. The weight data are typical values. The data points correspond with the year when the diameter was for the first time produced in larger numbers. Since 1970, the crystal diameter doubles approximately every 13 years while the average weight of the crystal doubles every 6 years



Fig. 4.2 *Left:* State of the art 300 mm diameter CZ Si ingot. Courtesy Siltronic AG. Ingots of this diameter weigh several hundred kilos. *Right:* First 450 mm diameter, dislocation free CZ Si ingot grown by SunEdison (Reprinted from [33], Copyright 2011, with permission from Elsevier. Courtesy SunEdison)

moment the pulling processes for the move to 450 mm are in full preparation [33, 86] but there is a clear delay of several years compared to what could be expected when extrapolating the data in Fig. 4.1. There are several reasons for this delay such as the development cost which increases very rapidly with increasing crystal diameter and also the uncertainty on the number of potential customers decreasing rapidly with increasing wafer diameter, the availability of suitable crystal pullers and 450 mm wafer characterization tools, and last but not least, the fact that one is now approaching the limit of what is possible based on the Si material properties as will become clear further in the chapter.

The main driver towards ever larger crystal diameters both for CZ and FZ Si crystal production has been reduction of cost per unit of wafer surface. While the CZ technique is coming close to what can be achieved with that respect, FZ crystal pulling might still be improved considerably as about 50 % of the cost of the crystal is due to the expensive polycrystalline Si feed rods. A new FZ-like technique was proposed using continuous feed of inexpensive Si granules instead of a feed rod [80].

For Ge substrates, the most used wafer diameter is 100 mm, although also 200 mm wafers are commercially available and 300 mm dislocation-free crystals

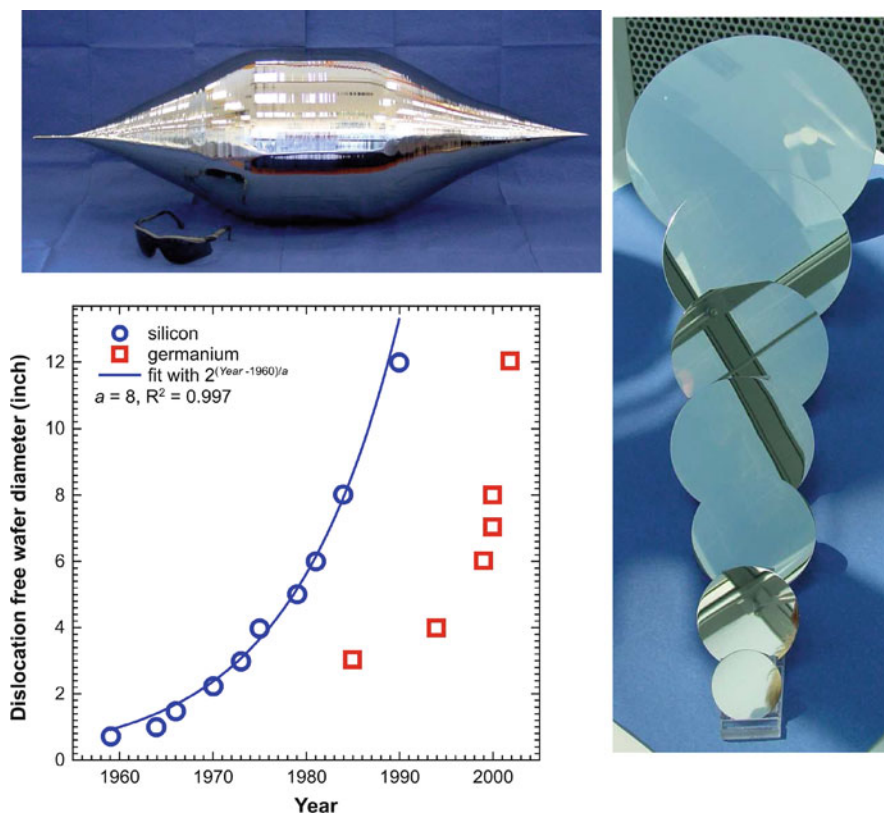


Fig. 4.3 *Top left:* One of the first 300 mm diameter, dislocation free Ge crystals, pulled in 2004. Courtesy Umicore Electro-Optic Materials (EOM). *Bottom left:* Very rapid development of dislocation-free 200 and 300 mm Ge wafers at Umicore EOM [47] compared with the wafer diameter development for CZ Si. *Right:* Electronic grade CZ Ge wafers with diameters ranging from 50 to 300 mm (Reprinted from [13], Copyright 2007, with permission from Elsevier. Courtesy Umicore EOM)

and wafers have been demonstrated as illustrated in Fig. 4.3 [13, 47]. In view of the limited Ge reserves available, application of Ge in mass-produced electronic components will always be under the form of thin Ge films mostly on large diameter Si substrates. One of the possibilities is to use the so called “smart cut” process to produce Ge On Insulator (GOI) wafers consisting of a thin mono-crystalline Ge film separated from a standard Si substrate by a thin silicon oxide layer [61]. For that purpose a high quality Ge “mother wafer” is needed with the same diameter as the Si substrate. This necessitated the development of 200 and 300 mm Ge crystal pulling and wafering processes.

4.2 Grown-in Defects in Single-Crystal Silicon Grown from a Melt

During the long history of single-crystal Si and Ge growth from a melt, grown-in defects have been a major concern. Initially the main problem was dislocation generation due to the thermal shock when dipping the crystal seed in the melt but this was soon solved by using the technique of Dash necking [9] leading to a complete removal of dislocations as illustrated in Fig. 4.4. After that, for a long time it was believed that grown-in defects were no longer an issue, all crystals were pulled fast enough to avoid dislocation clusters formed by self-interstitial “precipitation” during cooling of the pulled crystal. By the end of the 1980s, the device makers however noticed the presence of so called Crystal Originated Particles (COP’s) that were observed by wafer surface inspections tools based on visible light scattering after standard RCA wafer cleaning. The number of COP’s increased when repeating or extending the RCA cleaning hence it was concluded that the origin had to be the substrate. Closer investigation soon revealed that the so called particles were in fact crystallographic pits on the polished wafer surface [35] that formed by vacancy clustering during crystal cooling. As the COP’s were shown to lead to gate oxide degradation [36] it was quite important to improve the crystal pulling processes so that COP free wafers could be obtained. All commercial crystals in those days were

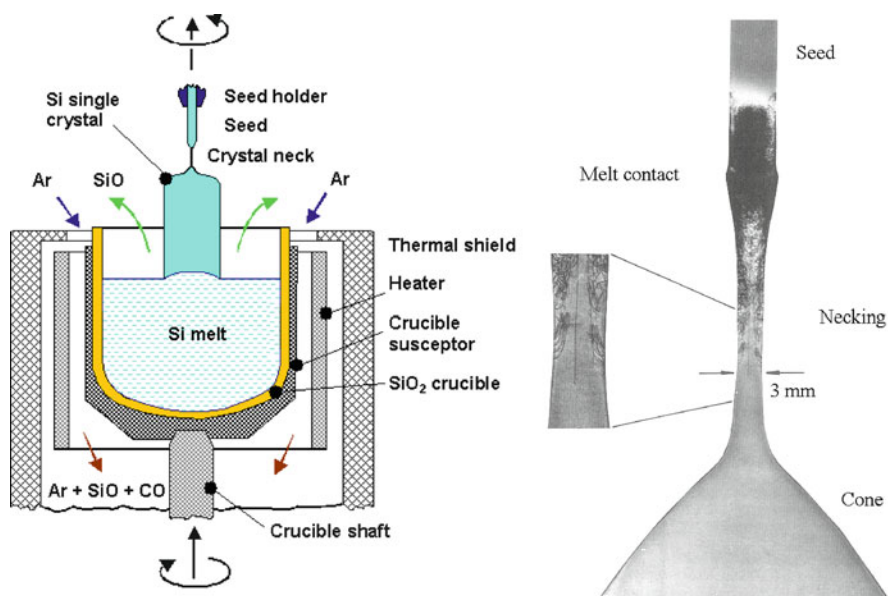


Fig. 4.4 Left: Schematic representation of the Czochralski pulling process [19]. Right: X-ray topographs showing dislocation removal by dash necking. Dislocations are formed due to the thermal shock when the seed touches the melt and glide out in the neck area [19]

vacancy-rich. Today's state of the art crystal pulling is aimed at COP and dislocation cluster free wafers.

4.2.1 State of the Art CZ and FZ Single-Crystal Pulling

Today the state of the art commercial single-crystal diameters are 300 mm for Czochralski pulled Si and Ge and 200 mm for Floating Zone (FZ) pulled Si (Figs. 4.2 and 4.5). As yet, no FZ pulling process for Ge is available. This is in

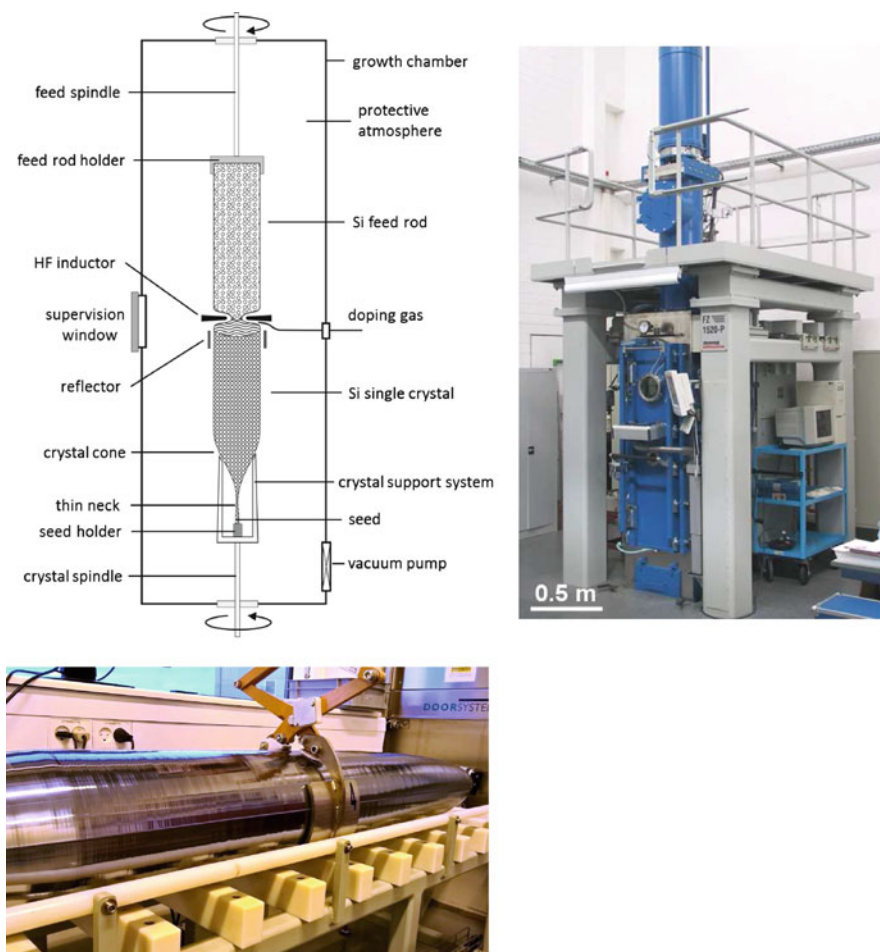


Fig. 4.5 Top left: Scheme of the FZ process for large-diameter Si single-crystals. Right: Puller for large diameter FZ crystal pulling at IKZ in Berlin [34] (Courtesy Robert Menzel). Bottom left: 8 in. FZ crystal, just taken out of the puller (Courtesy Topsil Semiconductor Materials)

part due to the larger weight of Ge, making it difficult to confine the molten zone during the FZ process. Recent attempts seem however promising and showed the feasibility to grow 35 mm diameter crystals [87]. The use of a magnetic field to contain the melt will probably be needed in order to make larger diameters FZ Ge crystal growth possible.

450 mm diameter CZ crystal pulling processes are being developed for Si (Fig. 4.2), requiring a more profound understanding of the various process parameters influencing intrinsic point defect behavior in order to be able to pull grown-in defect-free crystals using a commercially viable pulling process.

4.2.2 Experimental Observations on Grown-in Defects

4.2.2.1 Detection and Characterization of Grown-in Defects

Axial and radial distributions of grown-in defects in as-grown crystals can be observed using Cu decoration and X-ray topography as was already done in the early days of Si crystal growth from a melt using the Floating Zone or Czochralski pulling technique as illustrated in Fig. 4.6 [2, 4].

Grown-in defects can also be observed after using dedicated defect etching techniques. So called flow pattern defects (FPD's) and Secco etch pits (SEP's) are observed on wafer surfaces after immersion of the wafer piece with the polished surface in vertical position in unstirred Secco etchant for a prolonged etching time of the order of half an hour [88]. FPD's correspond with so called D-defects which are vacancy cluster related while SEP's are observed in regions that contain a lot of A-defects which are related to self-interstitial clusters. Although developed for moderately or low doped silicon substrates, a modified etch recipe can also be

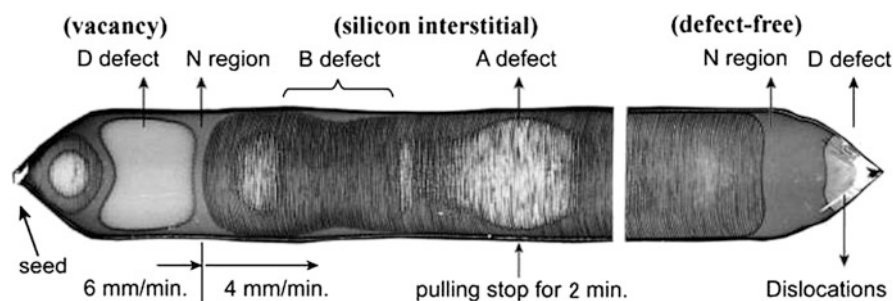


Fig. 4.6 X-ray topograph after Cu decoration of a 20 mm diameter FZ silicon crystal from seed to tail. During crystal growth, the pulling speed was varied while keeping the diameter constant resulting in vacancy type defect (D) and interstitial type defect (A and B) containing crystal parts as well as regions where no grown-in defects are observed (N region) (Reprinted from [4], Copyright 2011, with permission from Elsevier)

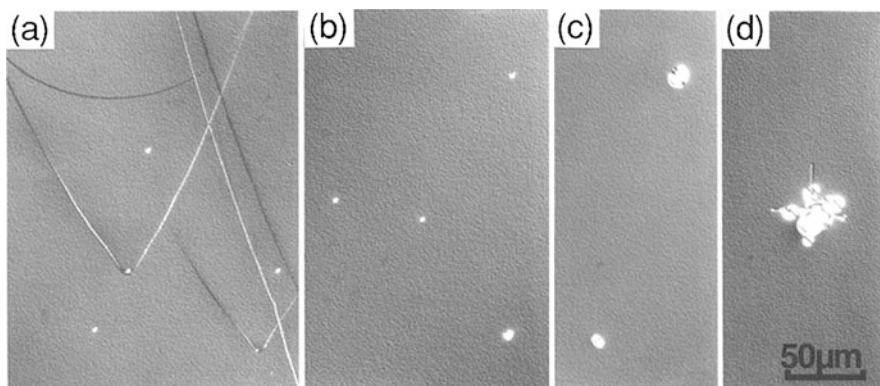


Fig. 4.7 Optical micro-graphs after FPD etching. Pulling rates of the 150 mm Si crystal: 1.1 mm/min (a) leading to a vacancy-rich crystal with D-defects that are revealed by FPD's; 0.7 mm/min, close to OSF-ring (b); outside OSF-ring (c) which is an interstitial-rich part of the crystal containing A-defects that are revealed as SEP's; 0.4 mm/min (d) leading to an interstitial-rich crystal containing a low density of dislocation clusters revealed as so called large pit defects [48] (Copyright 1993 The Japan Society of Applied Physics. Courtesy SUMCO)

applied for low resistivity wafers [89]. Examples of delineated A and D defects are shown in Fig. 4.7.

4.2.2.2 Vacancy Type Defects

Vacancy type grown-in defects in CZ Si or Ge are observed on polished wafer surfaces as so called Crystal Originated Particles (COP's) by wafer surface inspection tools based on the detection of scattered laser light by surface irregularities [68, 69, 74]. These advanced wafer surface inspection tools not only allow to detect and differentiate crystal defects from particles but also to determine the coordinates of these defects on the wafer surface. This makes it possible to investigate the nature of these defects using tools like scanning electron microscopy (SEM) or atomic force microscopy (AFM) after transfer of the defect coordinates to the sample/wafer holder of these instruments. This approach showed that the crystal defects observed on wafers prepared from vacancy-rich crystals are in reality crystallographic pits bounded by {111} planes that intersect the (001) wafer surface as a square with $\langle 110 \rangle$ edges. Often double pits are observed as show by the AFM images in Fig. 4.8. COP sizes in the range between 50 and 150 nm are commonly observed on Si wafers. The pit morphology and size are in good agreement with the octahedral voids that are observed by TEM (Figs. 4.9 and 4.10).

A similar approach but this time using a light scattering tool with an infra-red light laser beam, allows to detect and determine the 3D coordinates inside the silicon wafer of the lattice defects leading to COP formation on the polished wafer surfaces. Transferring the coordinates to focused ion beam specimen preparation tools for

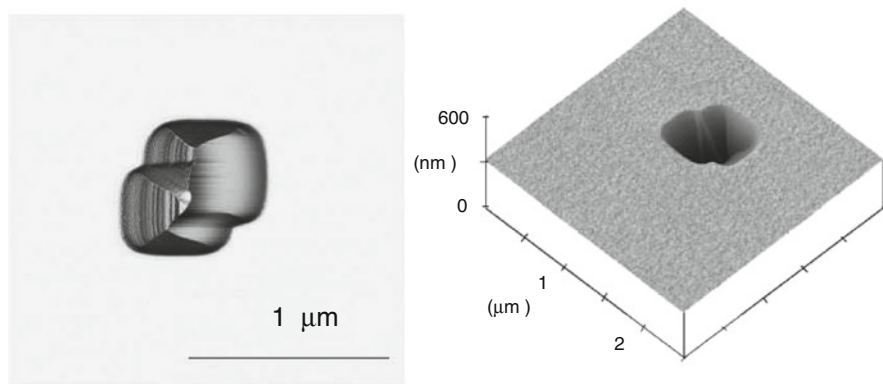


Fig. 4.8 AFM images of a typical double COP after 4h SC1 delineation. *Left:* top view. *Right:* 3D-view [68]

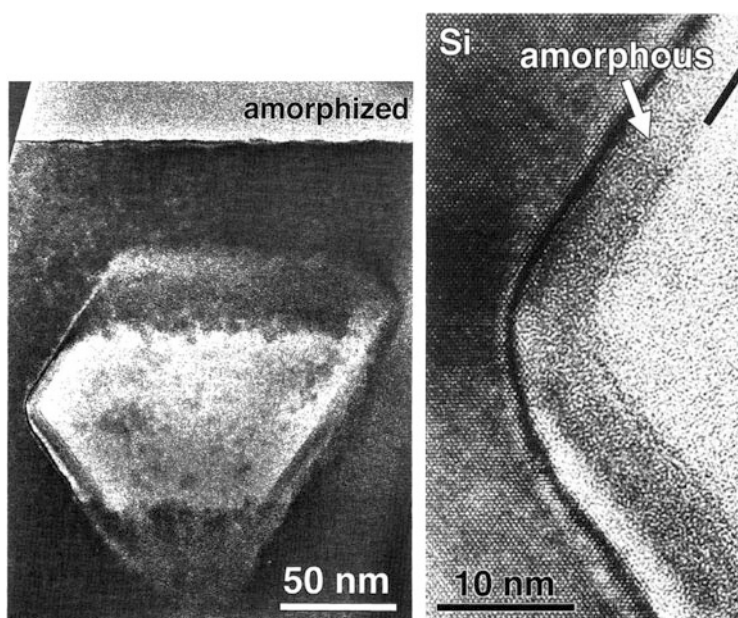


Fig. 4.9 *Left:* Cross-section TEM image of a void in CZ Si. *Right:* HREM image of the void/silicon matrix interface. A thin (≈ 10 nm) silicon oxide layer is formed during crystal cooling [8] (Copyright 1997 The Japan Society of Applied Physics)

transmission electron microscope (TEM) investigation, allows to study the nature of the defects in the as-grown crystal. An example of the observation of grown-in defects by infra-red light scattering tomography is shown in Fig. 4.11.

Common techniques for non-destructive bulk inspection of grown-in or processing induced point defect clusters such as cross-section infra Red Light Scattering

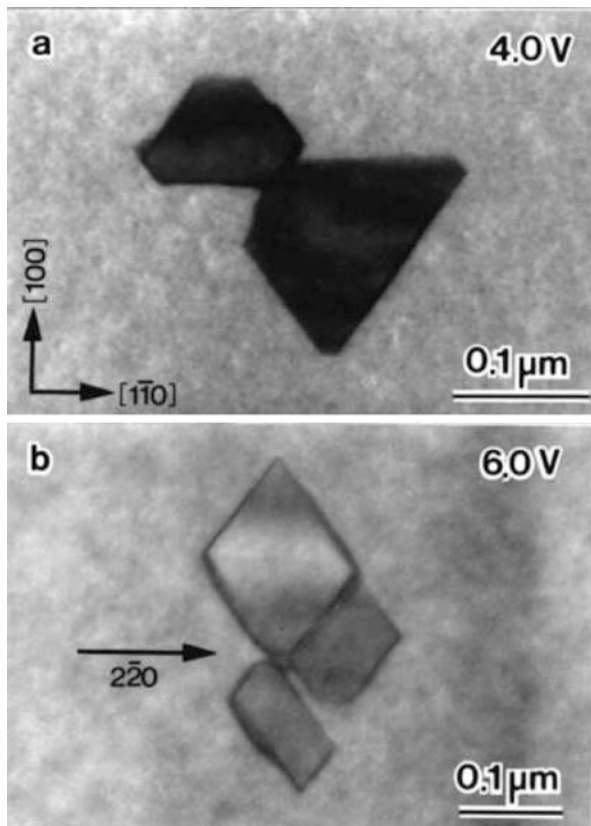


Fig. 4.10 TEM micrographs of grown-in voids in CZ Si grown at a pulling rate of 1.0 mm/min. *Top*: taken from the [110] pole. *Bottom*: taken with a $[2\bar{2}0]$ Bragg condition [25] (Copyright 1998 The Japan Society of Applied Physics)

Tomography (IR-LST) [28, 69], plan view inspection with a Scanning Infra Red Microscope (SIRM) which based on detecting backscattered light [76, 89, 90] or differential interference contrast microscopy [62], are based on scattering or interference of near infra red light in the 1–1.3 μm wavelength range for which Si is transparent.

When the size d of the light scattering defect is much smaller than the wavelength of the probing beam, Rayleigh scattering occurs and the Rayleigh scattering cross-section σ_s is given by [74]

$$\sigma_s = \frac{2\pi^5}{3} \frac{d^6}{\lambda^4} \left(\frac{n^2 - 1}{n^2 + 2} \right)^2, \quad (4.1)$$

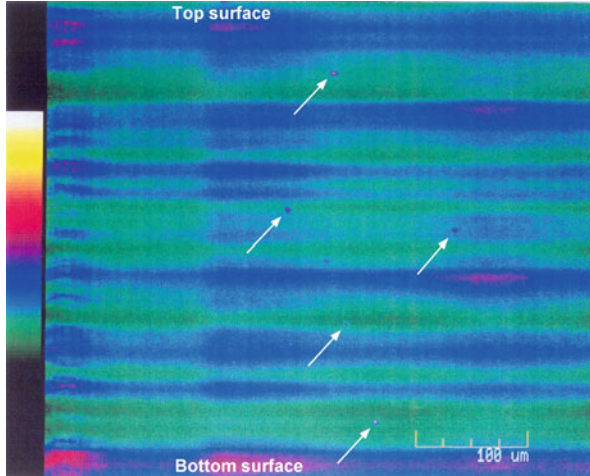


Fig. 4.11 IR-LST cross-section image of a cleaved wafer prepared from a vacancy-rich Si crystal revealing the presence of a large number of grown-in vacancy clusters indicated by arrows. The false color scale at the left corresponds with the scattering intensity and thus defect size, increasing from green to white (Courtesy Gudrun Kissinger)

with λ the wavelength of the probing light, n the refractive index of the particle material and d its diameter. From (4.1), and taking into account the difference in refractive index of the Si matrix and the defect phase, e.g. vacuum or SiO_2 , a lower size detection limit of about 20 nm (diameter) can be estimated for voids while that for oxide precipitates is only about 4 % larger.

When the inclusion is of the same order of magnitude or even larger than the wavelength of the probing light, assuming Mie scattering is a better approximation to describe the scattering process [74].

The advantage of working in backscattering like with SIRM is that measurements of grown-in void distributions [89] or oxide precipitate distributions after thermal treatments [90] are also possible on low resistivity material as illustrated in Fig. 4.12. The limited penetration depth should thereby be taken into account and corrections should be made for the reduced scattering intensity due to the increased light absorption in the substrate.

A typical void in as-grown CZ Si is e.g. shown in Fig. 4.9. The about 150 nm large void is a cluster of about 3×10^6 vacancies and the typical void density is of the order of $5 \times 10^6 \text{ cm}^{-3}$. This corresponds with a total vacancy concentration of the order of 10^{13} cm^{-3} , which is about 1 % of the thermal equilibrium vacancy concentration at melting temperature.

COP's are also observed on polished CZ Ge wafers (Fig. 4.13, right). They are typically one order of magnitude larger than those in Si. At the same time, the void density in CZ Ge is three orders of magnitude lower, suggesting a V thermal equilibrium concentration at melting temperature of the same order of magnitude as in Si.

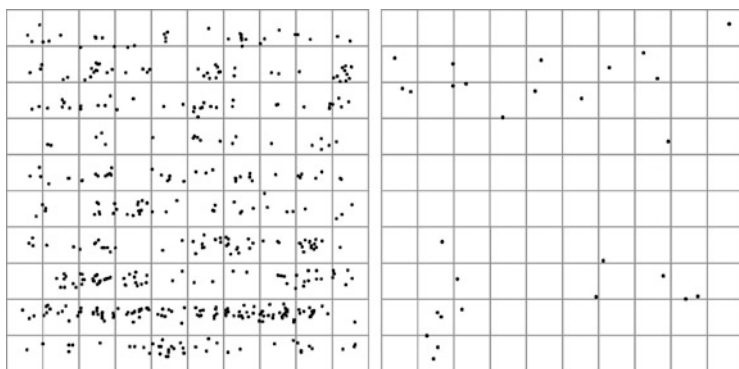


Fig. 4.12 Typical void maps obtained with SIRM in a $1.81.8\text{ mm}^2$ area in the center of two 100 mm diameter wafers. *Left:* $10^{20}\text{ Ge cm}^{-3}$ doped crystal. *Right:* Same type of crystal but co-doped with about $3 \times 10^{19}\text{ B cm}^{-3}$ (3–5 m Ωcm), after measuring a matrix of 10×10 adjacent areas of $180 \times 180\text{ }\mu\text{m}^2$ (Reproduced with permission from [89]. Copyright 2011, The Electrochemical Society)

In fast pulled crystals that are very vacancy-rich, the total concentration of vacancies incorporated in voids is nearly independent of the crystal cooling rate at 1120°C as illustrated in Fig. 4.14 [39].

4.2.2.3 Interstitial Type Defects

Interstitial type defects can be observed after Secco etching or after dislocation etching. In slow pulled crystals large etch pits are observed, corresponding with large dislocation clusters [48]. Such dislocations are very detrimental as they will propagate and multiply in epitaxial layers that are grown on such substrates [49]. A few typical examples are given in Fig. 4.15. The TEM image on the top shows a plan view of a large dislocation cluster in a slow pulled crystal [48]. The bottom micrographs show cross-section TEM images of dislocations in a $3\text{ }\mu\text{m}$ thick epitaxial layer grown on a polished wafer prepared from a slow pulled 200 mm diameter, low resistivity, B doped Si crystal. From the dislocation cluster size in the substrate and taking into account the Burgers vectors, it can be estimated that one grown-in defect contains about 10^{10} self-interstitials [49]. Taking into account that about $4 \times 10^3\text{ cm}^{-3}$ grown-in defects are observed by Secco etching, the total number of self-interstitials in the grown-in defects is about $4 \times 10^{13}\text{ cm}^{-3}$, which is again close to 1 % of the thermal equilibrium self-interstitial concentration at melting temperature taking into account the relatively large uncertainty on the number of self-interstitials in the grown-in dislocation.

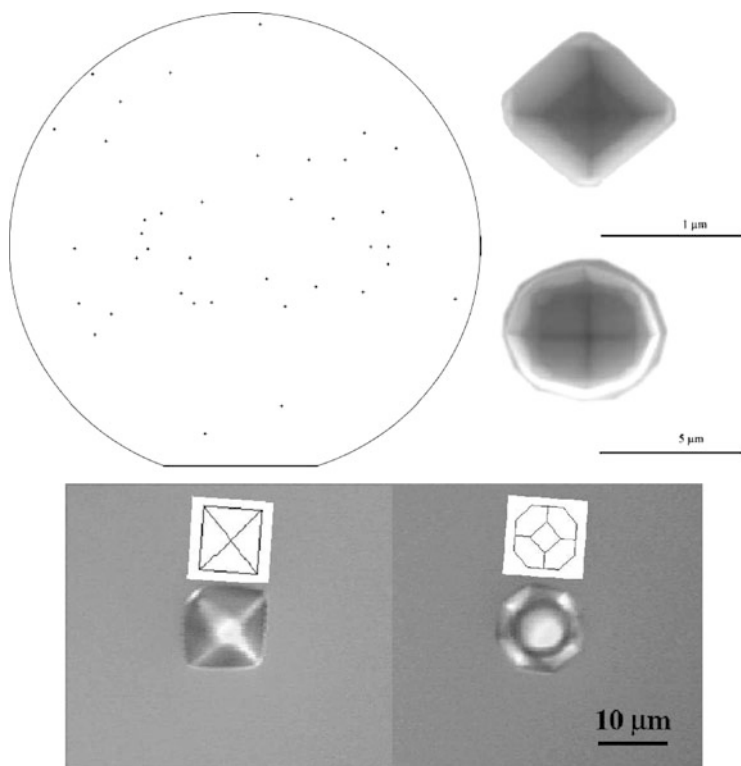


Fig. 4.13 *Left:* Wafer image obtained with a SURFSCAN surface inspection tool revealing the presence of a low density of large LPD's on a polished germanium wafer (Reprinted from [71], Copyright 2007, with permission from Elsevier). *Right:* SEM micro-graphs showing COP's corresponding with LPD's on the same wafer (Reprinted from [74], Copyright 2008, with kind permission from Springer Science and Business Media). *Bottom:* In extreme cases the COP's can be observed by the naked eye as strong light scatterers. Optical microscopy reveals a similar morphology as for the small COP's observed with SEM [22]. The COP's are formed by the intersection with the polished Ge wafer surface of large octahedral or truncated octahedral voids in the as-grown crystal

4.2.2.4 Transient Defect Phenomena

Abe and Takahashi [4] investigated the formation of grown-in defects in crystals grown with rapidly varying pulling rates. 50, 100 and 200 mm diameter crystals were grown in the same hot zone with a constant pulling rate of 1.0 mm/min until a steady state grown-in defect distribution was reached. Subsequently, the pulling rate was rapidly lowered to 0.3 mm/min, kept constant at that value for 30 min and then rapidly increased again to 1.0 mm/min.

Carrier lifetime maps of transversal sections of these crystals are shown in the top figure of Fig. 4.16 revealing the grown-in defect distributions. The OSF ring region is represented by the red area of low lifetime surrounded by narrow yellowish

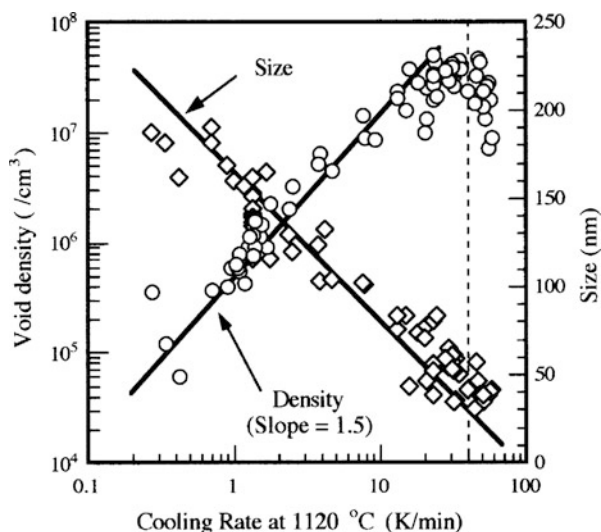


Fig. 4.14 Relationship between the crystal cooling rate at 1120 °C and the density and size of voids. The v/G value for the investigated crystals is more than double the critical value, yielding crystals that contain close to the maximum vacancy-concentration (Reprinted from [39], Copyright 2002, with permission from Elsevier)

regions of medium lifetime. Lifetimes are somewhat higher in the interstitial-rich region in the center, where interstitial clusters are present. Vacancy clusters are outside the OSF ring area where the lifetime is highest. The images also show that the interstitial-rich area extends well into the parts of the crystal where the original pulling rate of 1 mm/min was used and also that this extension is asymmetric.

Dornberger et al. [16] reproduced these experimentally observed features by simulation of the intrinsic point defect behavior (bottom figure of Fig. 4.16). They showed that the observations could be explained by an enhanced in-diffusion of self interstitials from the interface due to the lowered pulling rate. Resuming the original pulling rate generates a vacancy-rich crystal with the observed embedded ellipsoidal interstitial-rich areas in the 50 and 100 mm diameter crystals.

In another experiment, Abe and Takahashi [4] investigated the extreme case of pulling speed change by detaching the crystal from the melt. The results are shown in Fig. 4.17 revealing that even for a very slow pulled crystal that is thus very interstitial-rich after growth, a thin layer in which Anomalous Oxygen Precipitation (AOP) occurs can be observed close to the crystal-melt interface before detaching. AOP is an indication of a vacancy-rich crystal as the presence of a supersaturation of vacancies enhances oxide precipitate nucleation and growth. These detaching experiments clearly show that in all Si crystals pulled from a melt, the part of the crystal close to the melt is vacancy-rich with the axial extent of this vacancy-rich layer determined by the pulling rate and temperature gradient for the given hotzone.

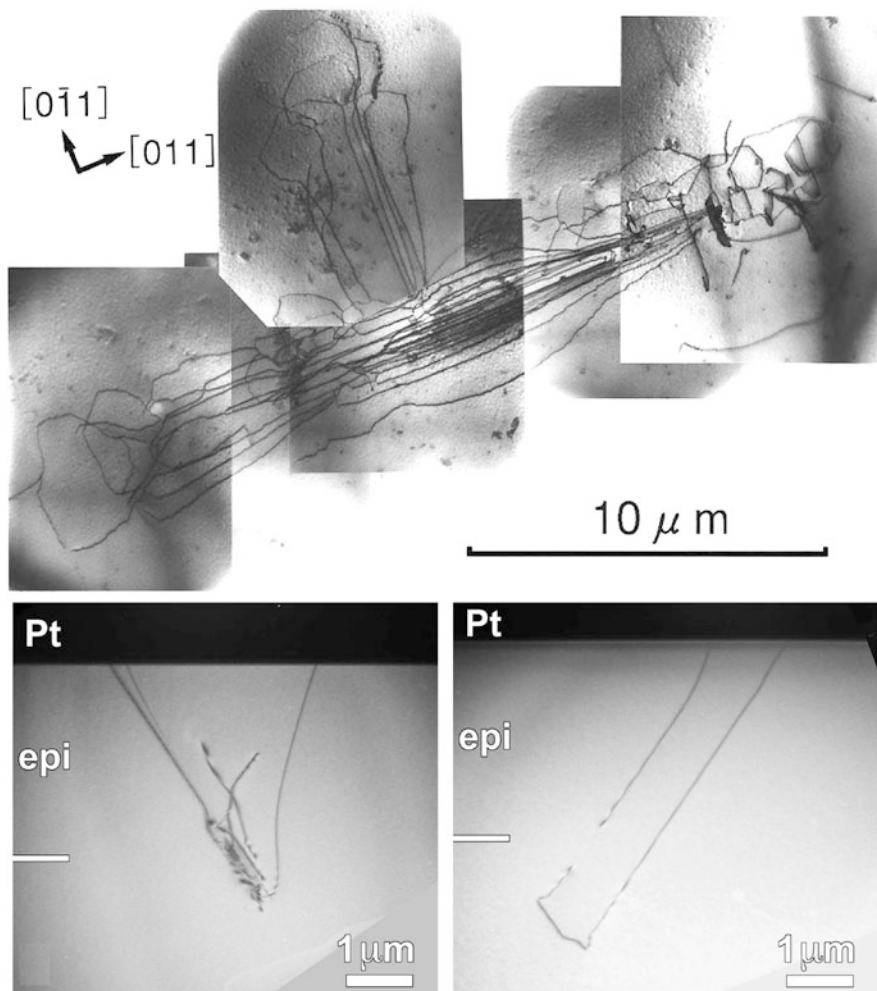


Fig. 4.15 *Top*: (100) plan view TEM image showing large dislocation clusters in a 150 mm Si crystal grown at 0.4 mm/min [48] (Copyright 1993 The Japan Society of Applied Physics. Courtesy SUMCO). *Bottom*: Cross-section TEM images of dislocations in a 3 μm thick epitaxial Si layer grown at 1100 $^{\circ}\text{C}$ on a wafer from a slow pulled 200 mm p^+ Si crystal. The dislocations nucleate at grown-in self-interstitial defects in the Si substrate [49] (Courtesy Hugo Bender, IMEC)

4.2.3 Simulation of Intrinsic Point Defect Cluster Formation During Crystal Pulling

Commercial simulators are available nowadays that allow a detailed simulation of the complete crystal growth process including temperature and thermal stress distributions, gas and melt flows and intrinsic point defect incorporation, distribution,

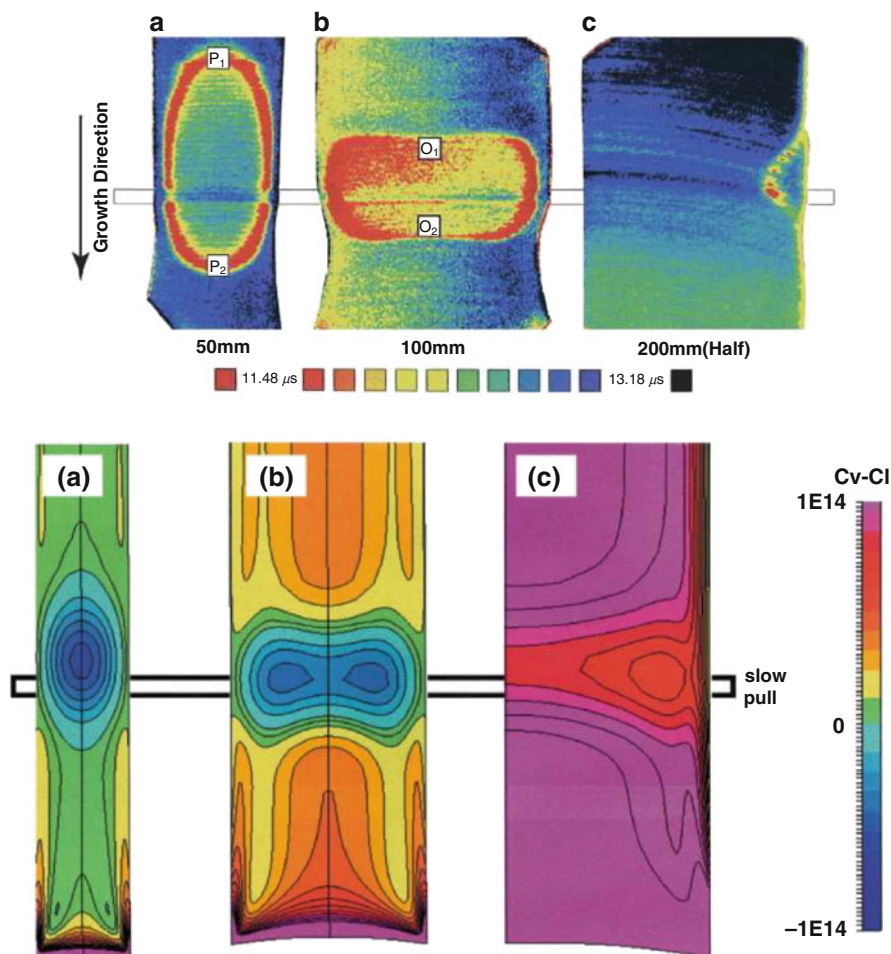


Fig. 4.16 Top: Minority carrier lifetime maps for 50 (a), 100 (b) and 200 mm (c) CZ silicon crystals grown with a pull rate of 1.0 mm/min and a temporary decrease to 0.3 mm/min (Reprinted from [4], Copyright 2011, with permission from Elsevier). Bottom: Simulated ($C_v - C_l$) distributions for the same crystal diameters and pulling conditions (Reprinted from [16], Copyright 2001, with permission from Elsevier)

recombination and clustering. This is illustrated in Fig. 4.18 (top) showing the result of a simulation of the formation of voids in Si and Ge by homogeneous nucleation of vacancy clusters which is driven by the increasing vacancy supersaturation during crystal cooling [22, 73]. The growth of the vacancy clusters is assumed to be vacancy diffusion controlled. The larger void/COP sizes in germanium compared to silicon are due to the much higher diffusivity of vacancies in germanium. Figure 4.18 (bottom) illustrates that good agreement can be obtained between measurement and simulation.

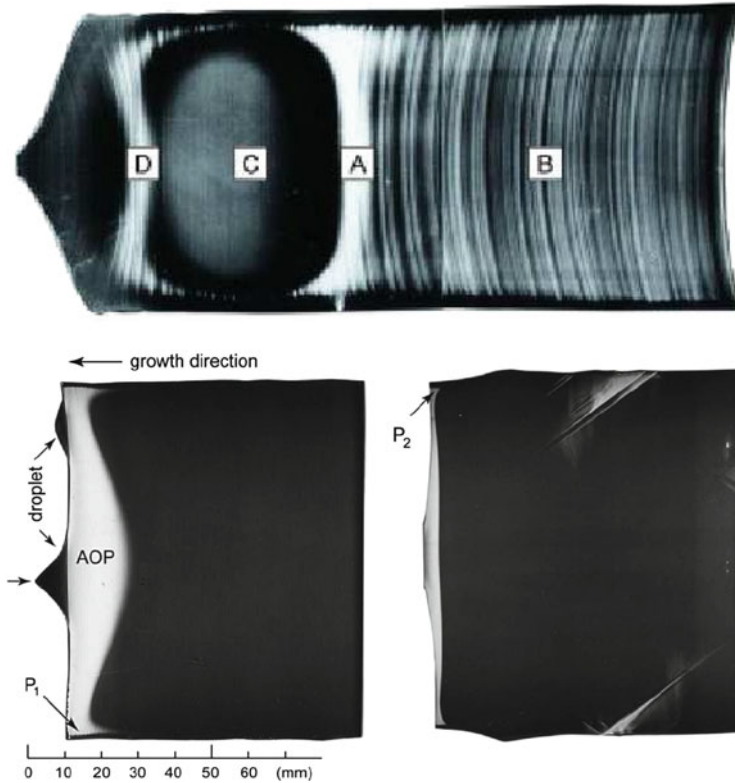


Fig. 4.17 *Top*: AOP in a fast pulled detached 70 mm CZ crystal (1.5 mm/min, vacancy-rich). *Bottom left*: AOP in a medium speed pulled detached 105 mm CZ crystal (0.47 mm/min, interstitial-rich). *Bottom right*: AOP in a slow pulled detached 110 mm CZ crystal (0.15 mm/min, very interstitial-rich) (Reprinted from [4], Copyright 2011, with permission from Elsevier)

Despite this good agreement between simulation and measurement for the various models reported in literature, it should be mentioned at this stage that the point defect properties that are extracted from a best fit between experimental data and simulation, can vary widely depending on the model that is used to simulate the crystal pulling process and the point defect clustering.

A good illustration of this uncertainty on the properties of both intrinsic point defects is the value of the recombination coefficient k_{IV} between vacancies and self-interstitials. In processes such as crystal pulling, plastic deformation and ion implantation, both types of intrinsic point defects are generated and/or coexist. An important parameter controlling the concentration of both point defects is k_{IV} which is given by the well-known expression

$$k_{IV} = 4\pi a_c(D_V + D_I) \exp[-\Delta G_{rec}/kT], \quad (4.2)$$

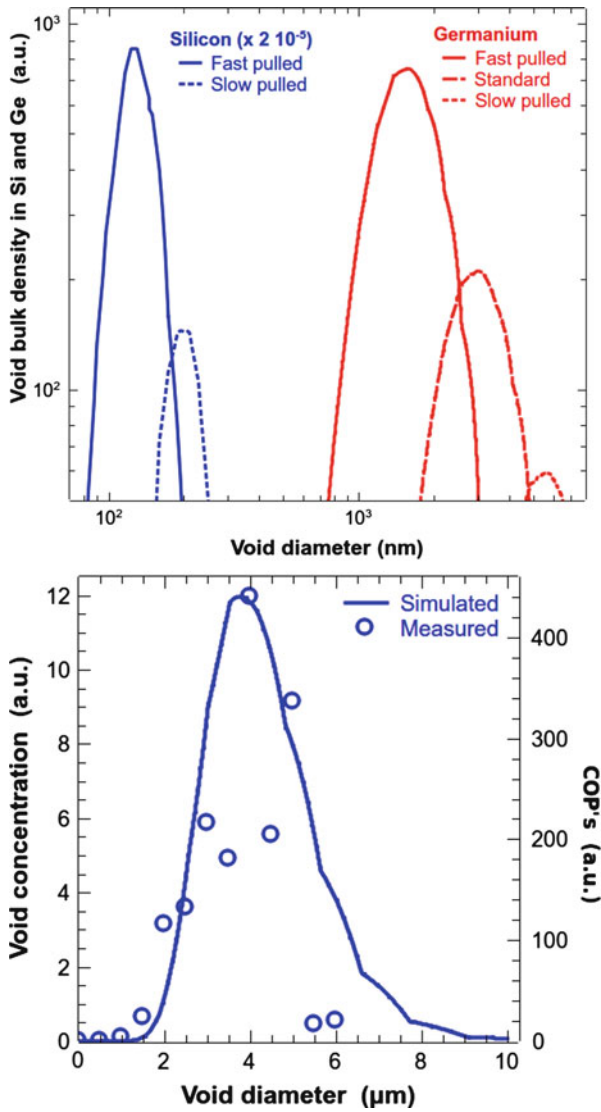


Fig. 4.18 *Top:* Simulated void size/density distributions in Si and Ge, illustrating the impact of crystal pulling speed. The simulations also predict the observed one order of magnitude larger void size in Ge which is associated with a three orders of magnitude lower volume density [73, 75] (Reprinted from [73], Copyright 2008, with permission from Cambridge University Press). *Bottom:* Comparison between measured COP distribution on a polished Ge wafer and the simulated distribution of voids in the bulk [22]. The COP distribution was measured using a confocal review station

with a_c the capture radius of the order of 1 nm and ΔG_{rec} the free energy barrier against recombination.

Assuming an Arrhenius-type behavior, k_{IV} can also be written as [32]

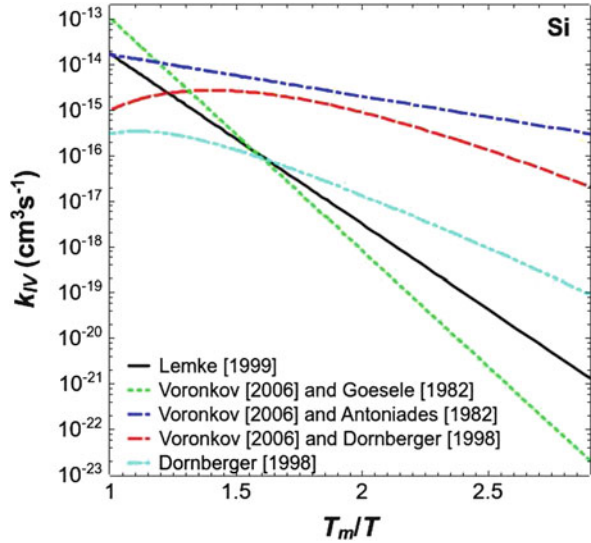
$$k_{IV} = k_m \exp[-(E_{rec}/kT_m)(T_m/T - 1)], \quad (4.3)$$

with k_m a constant and E_{rec} the activation energy for recombination.

Applying (4.2) and (4.3) for data obtained from grown-in defect distributions in floating zone and Czochralski grown Si crystals [18, 30], yields the k_{IV} dependence on the temperature normalized to the melt temperature as shown in Fig. 4.19. It is clear that a large uncertainty (still several orders of magnitude near the melting temperature) exists with respect to the value of k_{IV} and that it strongly depends on the model that is used to simulate the crystal growth process. For Ge, data for the self-interstitial are to a large extent still lacking making it very difficult to estimate the recombination factor.

To some extent the crystal pulling process and defect simulators should therefore be considered as sophisticated extra- or interpolation tools. Only a further refinement of the physical models used in the simulators will allow to extract more reliable intrinsic point defect properties from the fit to the experiments.

Fig. 4.19 k_{IV} in Si as a function of the temperature normalized with respect to the melting temperature [72, 73] (Reprinted from [73], Copyright 2008, with permission from Cambridge University Press)



4.2.4 The Voronkov Criterion for Defect-Free Crystal Growth

Already in 1982, Voronkov presented a model describing intrinsic point defect behavior during the growth of single-crystal silicon from a silicon melt and derived a criterion to predict if the crystal was vacancy- or self-interstitial-rich [82]. The “Voronkov criterion” was further refined in the following decades [84] and is based on the experimental observation that the intrinsic point defect balance near the crystal-melt interface is determined by Γ , the ratio of pulling speed v over temperature gradient G at the crystal-melt interface. When this ratio is larger than a critical value Γ_{crit} , the crystal is vacancy-rich; when the ratio is below the critical value, the crystal is self-interstitial-rich. Published values for Γ_{crit} range between 1.3 and $2.2 \times 10^{-3} \text{ cm}^2 \text{ min}^{-1} \text{ K}^{-1}$ and depend among others on the simulator that is used to calculate the thermal gradient and also on the doping and resistivity of the crystal [14, 15, 23, 31, 81, 83]. The Voronkov model has been widely accepted and is used in crystal pulling simulators, allowing to predict intrinsic point defect clustering in single-crystal silicon grown by the Czochralski or floating zone techniques. The growth of so called perfect silicon crystals up to 300 mm diameter, without observable intrinsic point defect clusters is largely based on the application of the Voronkov criterion.

Despite the success in applying the Voronkov criterion to improve crystal quality there are also a number of remarks on its validity. Abe claimed already 30 years ago that the axial thermal gradient G near the crystal-melt interface in growing FZ and CZ silicon crystals decreases with increasing pulling speed instead of increasing, as mostly assumed [1, 3, 5]. The FEMAG simulator predicts that G increases with decreasing pulling rate [81], while other simulators give opposite results [60]. This also suggests that the pulling speed and the thermal gradient might not be independent parameters in the Voronkov criterion.

Another issue with the Voronkov criterion is that the influence of the stress introduced by the thermal gradient at the crystal-melt interface on the intrinsic point defect formation enthalpy is not explicitly taken into account. As the thermal stress increases with crystal diameter, this might become an important issue in the development of 450 mm diameter Si crystals.

Application of the criterion for the development of even larger diameter crystals and for heavily doped crystals needs thus a better understanding of the various material and crystal pulling process parameters that influence the intrinsic point defect properties and thus also the value of Γ_{crit} . A side effect would also be that more accurate intrinsic point defect parameter could be extracted from grown-in defect studies in dedicated as-grown crystals, even using smaller diameters thus making the experiments less expensive. This paper discusses the present state of understanding of the impact of these parameters and also further work that is needed to improve the Voronkov criterion for ultra large diameter crystals.

4.2.4.1 Intrinsic Point Defect Diffusion and Recombination

The diffusion and recombination reaction of point defects during the crystal growth process can be described by Eqs. (4.4), (4.5), (4.6) and (4.7) [29, 40, 43, 51, 52].

$$J_V = -D_V \nabla C_V - \frac{D_V C_V Q_V^*}{k_B T} \nabla T \quad (4.4)$$

$$J_I = -D_I \nabla C_I - \frac{D_I C_I Q_I^*}{k_B T} \nabla T \quad (4.5)$$

$$\frac{\partial C_V}{\partial t} = -\nabla J_V - v \frac{dC_V}{dz} - k_{IV} (C_V C_I - C_V^{eq} C_I^{eq}) \quad (4.6)$$

$$\frac{\partial C_I}{\partial t} = -\nabla J_I - v \frac{dC_I}{dz} - k_{IV} (C_V C_I - C_V^{eq} C_I^{eq}) \quad (4.7)$$

where J is the diffusion flux, C is the actual concentration of the point defect and the subscripts V and I denote the vacancy and self-interstitial, respectively. T is absolute temperature and k_B is the Boltzmann constant. The second term in the right part of Eqs. (4.4) and (4.5) expresses the effect of the temperature gradient on the diffusion. Q^* is the reduced heat of transport. The second term in the right part of Eqs. (4.6) and (4.7) denotes the effect of the crystal pulling on the concentrations with v the pulling rate of the crystal. The third term in the right part of Eqs. (4.6) and (4.7) describes the recombination reaction between V and I with k_{IV} the reaction constant given by (4.2).

C^{eq} and D depend exponentially on temperature

$$C_{I,V}^{eq}(T) = C_{I,V}^0 \exp\left(-\frac{E_{I,V}^f}{k_B T}\right) \quad (4.8)$$

$$D_{I,V}(T) = D_{I,V}^0 \exp\left(-\frac{E_{I,V}^m}{k_B T}\right), \quad (4.9)$$

with $E_{I,V}^f$ and $E_{I,V}^m$ the intrinsic point defect formation and migration energies, respectively. $C_{I,V}^0$ and $D_{I,V}^0$ are the corresponding pre-factors.

Table 4.1 lists recent parameters of the intrinsic point defects in silicon crystal derived from the analysis of grown-in defect patterns [29, 43, 46, 51]. These values reported in literature fall within a relatively narrow range. Figure 4.20 shows the corresponding $C_{I,V}^{eq}$ and $D_{I,V}$ as function of the temperature. In the same figure also the transport capacity $C_{I,V}^{eq} D_{I,V}$ is shown, revealing a cross-over between 800 and 950 °C. At higher temperature the transport capacity of the interstitial is larger than that of the vacancy and vice versa below that temperature. It is this cross-over that is the reason that the Voronkov criterion “works”. The transport capacities calculated with the Nakamura et al. [43] and the Nishimo et al. [46] data nearly coincide.

Figure 4.21a, b show the axial distributions of V and I concentration for the case of low v/G condition and high v/G condition, respectively. The parameters of point

Table 4.1 Intrinsic point defect parameters in silicon derived from grown-in defect distributions

	[43]	[51]	[29]	[46]
$C_V^{eq}(T_m) (\times 10^{14} \text{ cm}^{-3})$	6.49	8.73	8.40	4.58
$C_I^{eq}(T_m) (\times 10^{14} \text{ cm}^{-3})$	4.84	7.1	6.89	3.17
$D_V(T_m) (\times 10^{-5} \text{ cm}^2 \text{ s}^{-1})$	4.45	3.4	4.0	6.31
$D_I(T_m) (\times 10^{-4} \text{ cm}^2 \text{ s}^{-1})$	5.0	3.76	4.0	7.66
E_V^f (eV)	3.94	3.70	4.00	3.84
E_I^f (eV)	4.05	4.00	4.00	3.77
E_V^m (eV)	0.3	0.457	0.4	0.4
E_I^m (eV)	0.9	0.937	0.9	1.18
Q_V^* (eV)	0	0	0	0
Q_I^* (eV)	1.01	0	0	0
$C_V^{eq}(T_m) - C_I^{eq}(T_m) (\times 10^{14} \text{ cm}^{-3})$	1.7	1.6	1.51	1.41

defects that were used are the values of Nakamura et al. [43] in Table 4.1. We can see that self-interstitial becomes the dominant species at the steady state away from the crystal-melt interface in the case of small v/G condition and that the vacancy becomes the dominant species in the case of large v/G condition.

Figure 4.22 shows the relationship between v/G and point defect concentrations at the steady state. We can see that there is a critical v/G at which the dominant species changes. Both concentrations of vacancy and self-interstitial become very low at $[v/G]_{crit}$. Therefore, the grown-in defect-free crystals can be grown under the condition of $[v/G]_{crit}$.

Voronkov and Falster have derived Eq. (4.10) for $[v/G]_{crit}$ at which J_V and J_I from the crystal-melt interface to the crystal become equal [84].

$$\left(\frac{v}{G}\right)_{crit} = \frac{D_I(T_m)C_I^{eq}(T_m)(E + Q_I^*) - D_V(T_m)C_V^{eq}(T_m)(E + Q_V^*)}{[C_V^{eq}(T_m) - C_I^{eq}(T_m)]k_B(T_m)^2} \quad (4.10)$$

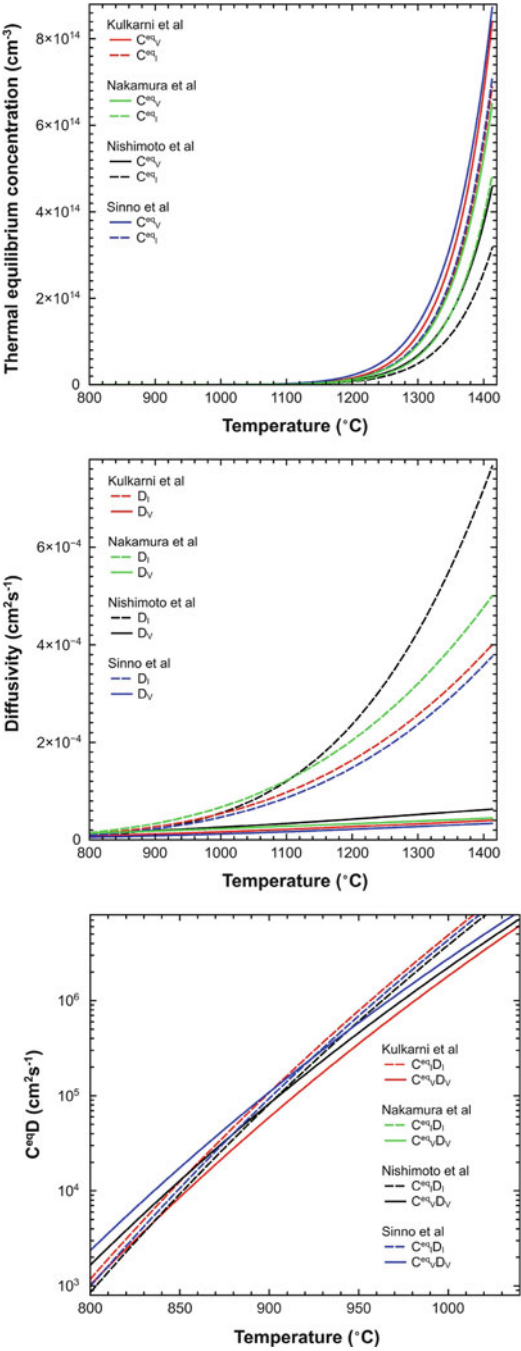
with

$$E = \frac{E_V^f + E_I^f}{2}.$$

T_m is the melting temperature, C^{eq} the equilibrium concentration and E^f the formation energy of the intrinsic point defect. Q^* is the reduced heat of transfer which is not very well known with values in literature ranging between 0 and $-E^f$ [38] in agreement with the expression derived for Q^* by Tan [59]

$$Q^* = E^m - E^f + k_B \ln \frac{C}{C^{eq}}. \quad (4.11)$$

Fig. 4.20 Thermal equilibrium concentrations (*top*) and diffusivities (*middle*) of the vacancy and the self-interstitial corresponding with the point defect parameters of Table 4.1 [29, 43, 46, 51]. *Bottom*: Transport capacity $C^{eq}D$ as function of temperature. At high temperatures the transport capacity of the self-interstitial is larger, at low temperatures that of the vacancy



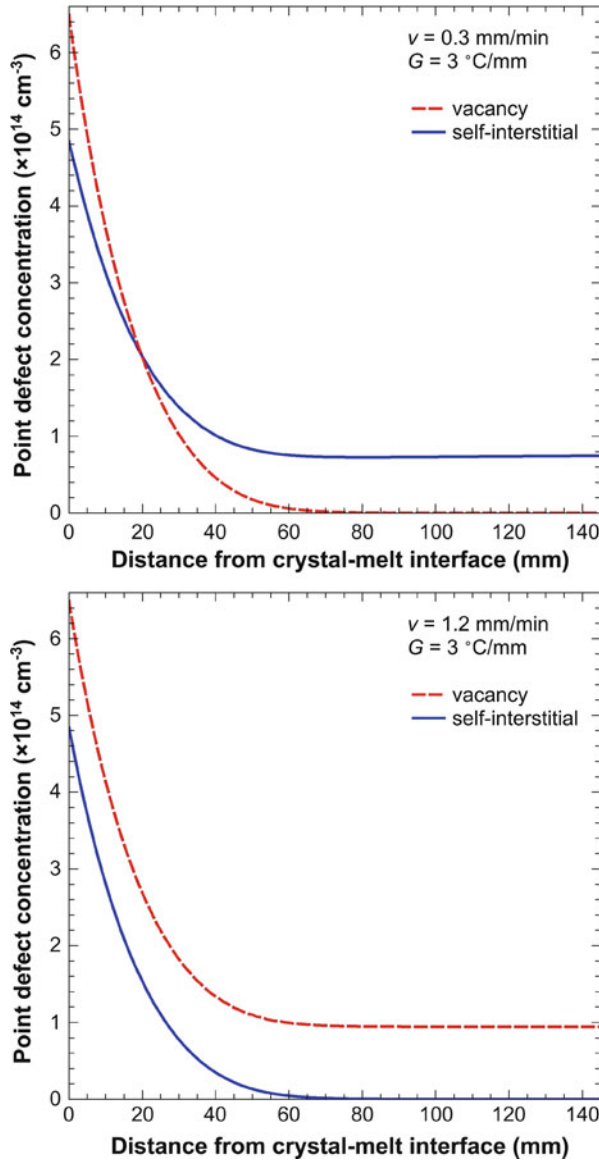


Fig. 4.21 Axial distribution of point defect concentrations during crystal growth. *Top*: Self-interstitial dominant condition (small v/G). *Bottom*: Vacancy dominant condition (large v/G) [37]

Neglecting the possible impact of Q^* , a more simple expression can be derived for the Voronkov criterion [66]

$$\left(\frac{v}{G}\right)_{crit} = \frac{D_I(T_m)C_I^{eq}(T_m)E_I^f - D_V(T_m)C_V^{eq}(T_m)E_V^f}{[C_V^{eq}(T_m) - C_I^{eq}(T_m)]k_B(T_m)^2} \quad (4.12)$$

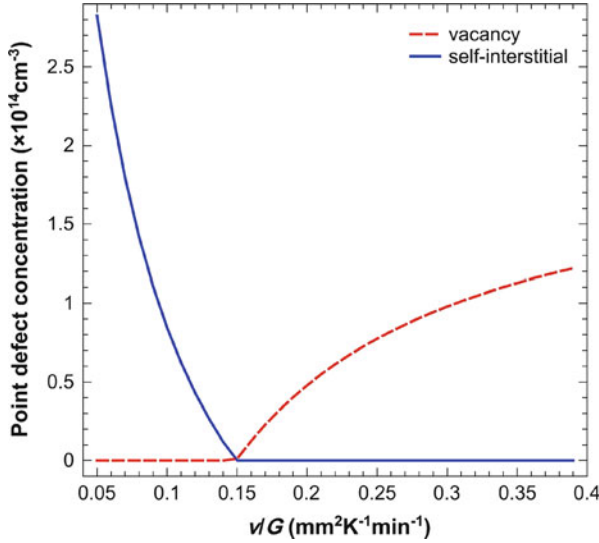


Fig. 4.22 Relationship between v/G and point defect concentrations at the steady state in the sufficiently distance away from the crystal-melt interface [37]

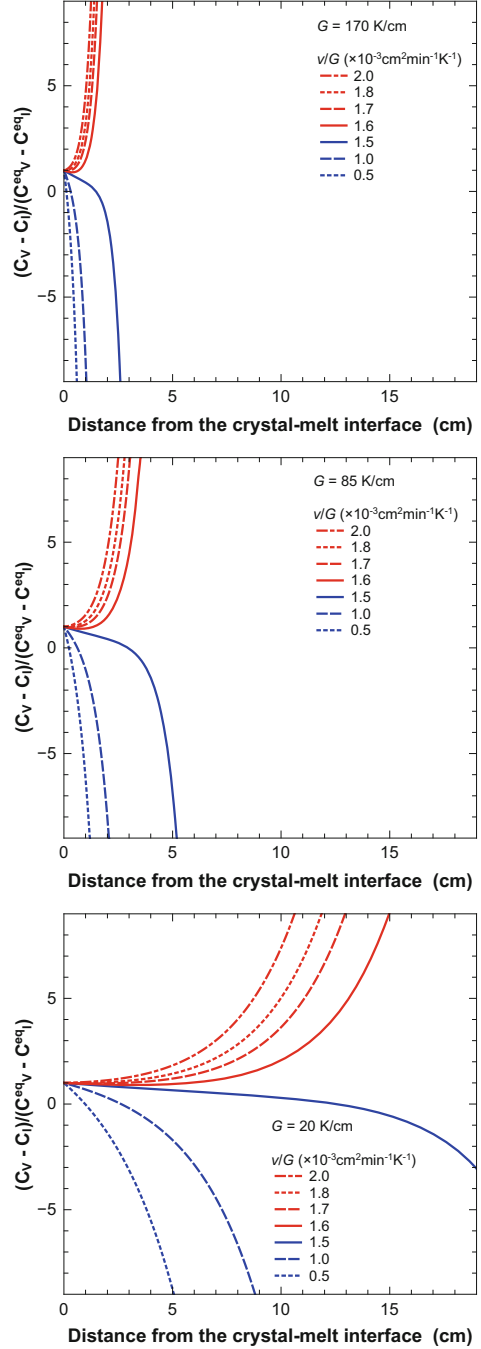
$[v/G]_{crit}$ is only determined by the physical parameters of the point defects as shown in the right hand side of Eqs. (4.10) and (4.12). Grown-in-defect-free crystals basically can be grown by controlling v/G near the critical value at all radial positions. Ideally this means that G is constant in the radial direction and v can then be calculated from Eqs. (4.10) or (4.12), using the appropriate intrinsic point defect parameters.

An example of result of the calculation of the relative point defect concentration difference $(C_V - C_I)/(C_V^{eq} - C_I^{eq})$ using Eq. (4.12) is shown in Fig. 4.23 illustrating that for all crystals, even the most interstitial-rich ones, there is a layer close to the crystal-melt interface that is vacancy-rich [66]. The thermal gradients of 170, 85 and 20 K/cm correspond roughly with crystal diameters of 50, 100 and 300 mm, respectively. The simulation results suggest that for interstitial-rich crystals pulled close to $[v/G]_{crit}$, the vacancy-rich layer can easily extend over a distance of the order of the crystal radius from the crystal-melt interface.

Equations (4.10) and (4.12) are, however, derived by using a one dimensional diffusion model. That is a good approximation near the crystal center where the crystal-melt interface is quasi flat. At other radial positions, the crystal-melt interface is however curved and due to that, the intrinsic point defect diffusion from the crystal-melt interface has a radial component. This radial component is determined not only by the interface curvature but also by radial out diffusion towards the free surface the crystal. The effect of the crystal-melt interface shape on $[v/G]_{crit}$ is discussed in next section based on the use of Eq. (4.10).

Fig. 4.23

$(C_V - C_I)/(C_V^{eq} - C_I^{eq})$ as function of the distance from the crystal-melt interface with v/G as parameter without taking stress effects into account for three different thermal gradients G [66]. The figures illustrate that the crystal remains free from point defect clusters over a length which depends on v/G and on G (and thus also on the crystal radius). Furthermore, for all diameters and pulling conditions, the crystal is vacancy-rich, corresponding with $(C_V - C_I)/(C_V^{eq} - C_I^{eq}) > 0$, close to the crystal-melt interface. This explains the observations shown in Fig. 4.17



Besides the curved crystal-melt interface, also material or process parameters affecting the intrinsic point defect thermodynamic parameters, will change the value of $(v/G)_{crit}$. The impact of thermal stress and of dopants will be discussed in the final part of the chapter.

4.3 Impact of the Crystal-Melt Interface Shape on v/G

4.3.1 Change of the Critical v/G by the Interface Shape

$[v/G]_{crit}$ changes by the shape of the crystal-melt interface [40, 43] as illustrated in Fig. 4.24, showing the relationship between $[v/G]_{crit}$ and the inverse radius of curvature of the interface at the crystal center of 200 mm diameter crystals with different interstitial oxygen concentration. In first order approximation, $[v/G]_{crit}$ is inversely proportional to the radius of curvature of the interface. This phenomenon has been explained by simulating the intrinsic point defect behavior in a growing crystal [40].

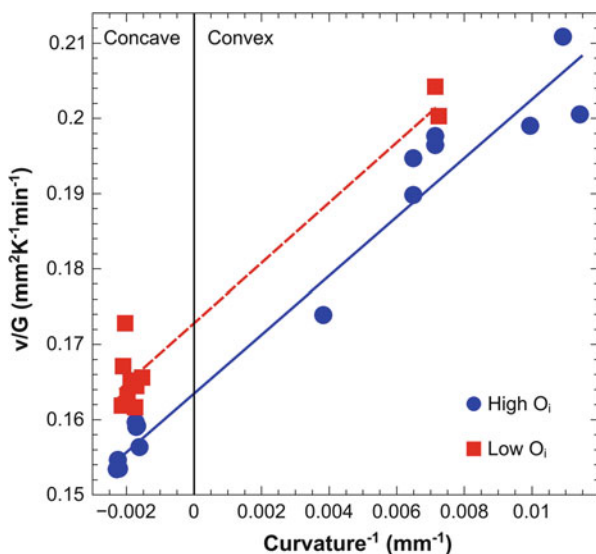


Fig. 4.24 Relationship between $(v/G)_{crit}$ at the crystal center and the radius of curvature of the crystal-melt interface for two interstitial oxygen concentrations (high: $> 13 \times 10^{17} \text{ O}_i/\text{cm}^3$; low: $< 13 \times 10^{17} \text{ O}_i/\text{cm}^3$, old ASTM) [40, 43]

4.3.2 Temperature Gradient Distribution Dependence on Interface Shape

Numerical simulation shows that the radial distribution of G changes with the shape of the crystal-melt interface. The boundary conditions that determine the temperature distributions in the crystal are the temperature distribution at the crystal periphery and at the crystal-melt interface. Because the temperature at the crystal-melt interface is the melting temperature, the shape of crystal-melt interface and the temperature distribution at the crystal periphery determine the temperature distribution in the crystal. For a series of crystal-melt interface shapes, the G distribution at the interface was calculated using the same temperature distribution at the crystal periphery. Results are shown in Fig. 4.25 illustrating that G is quite sensitive to the interface shape and thus also v/G .

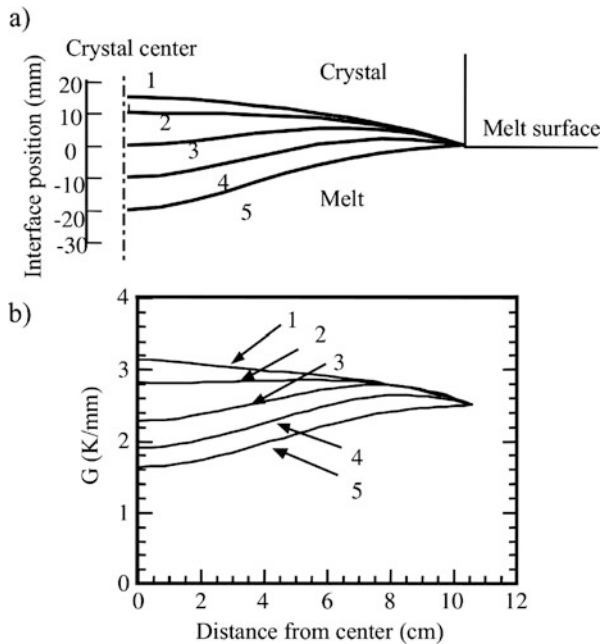


Fig. 4.25 Dependence of the axial thermal gradient G on the interface shape *top*: crystal-melt interface shapes that were studied. *Bottom*: Calculated radial G profiles. The temperature distribution of the crystal outer surface is assumed to be T (in K) = $1685 - 2.5 \times z$, with z (in mm), the distance along the crystal axis direction [37]

4.3.3 Change of the Interface Shape by the Pulling Condition

The interface shape is thus an important factor for the control of intrinsic point defect incorporation as shown in the previous paragraph. The interface shape itself is determined by the balance of heat fluxes in the crystal and the melt and by the latent heat at the crystal-melt interface. Figure 4.26 shows the relationship between the interface height at the crystal center and the average v/G ($[v/G]_{ave}$) for a 200 mm diameter silicon crystal using horizontal magnetic fields with different strengths [50].

G_{ave} is the average axial temperature gradient defined in Fig. 4.26 and represents the heat extraction capacity of the CZ furnace and hot zone. As the heat flux in the melt changes with the strength of the horizontal magnetic field, the dependence of the interface height on v/G_{ave} also changes with the horizontal magnetic field.

It was found that v/G can be used to predict the height h of the crystal-melt interface, according to the semi-empirical linear equation [50]

$$h = \frac{\alpha H}{\lambda_S} \frac{v}{G} + a(\alpha - 1) + b. \quad (4.13)$$

Hereby, α is a parameter that depends on the crystal diameter, H the latent heat and λ_S the thermal conductivity of the Si crystal. a and b are fitting parameters which can be obtained statistically for a given crystal diameter and magnetic field by analyzing many sets of actual interface heights and calculating the corresponding

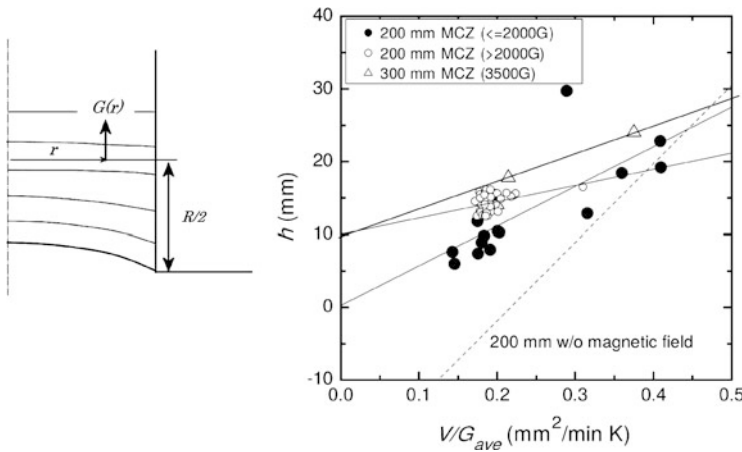


Fig. 4.26 Left: Schematic representation used for the definition of the average temperature gradient $G_{ave} = [2\pi \int_0^R G(r)]/[\pi r^2]$. Right: The relationship between the experimental interface height h and $[v/G]_{ave}$ for 150, 200 and 300 mm Si crystals grown with magnetic fields of different strengths. The dashed line is for a 200 mm crystal grown without magnetic field (Reprinted from [50], Copyright 2004, with permission from Elsevier)

temperature distributions for various types of hot-zones under different process conditions.

in addition, it is possible to estimate the maximum crystal growth rate v_{max} for a given hot zone from [50]

$$v_{max} = \frac{\alpha \lambda G}{(1 - \alpha)H}. \quad (4.14)$$

4.4 Simulation of Intrinsic Point Defects During Crystal Growth

The optimum condition for pulling a grown-in defect-free crystal was determined based on intrinsic point defect simulations [40]. First, the results of the point defect simulation were compared with the experimental observations on grown-in intrinsic point defect cluster distributions. The temperature distribution was estimated by a global heat transfer analysis method that took the melt convection into account and fitted the shapes of the crystal-melt interface in the calculations to the actual shapes using a turbulence parameter [40, 43]. The FEMAG simulation code was used for the calculation of the temperature field with the Mixing-Length (M-L) model to take into account convection [17]. The shape of the crystal-melt interface was also evaluated experimentally by investigating the growth striations using X-ray topography.

Figure 4.27 shows how changes in the growth rate influence the distribution of the defect regions for an almost uniform G in the radial direction. Figure 4.27a shows the change in the growth rate and Fig. 4.27b shows a cross section X-ray topograph of a crystal after thermal annealing. When the growth rate is decreased, the OSF ring closes and self-interstitial type dislocation clusters appear. Regions with and without oxygen precipitates can be seen between the OSF ring and the so called B band. These regions are called P_V (vacancy rich grown-in-defect-free region) and P_I (self-interstitial rich grown-in-defect-free region), respectively. The boundary between the two regions is the actual transition between the V -rich and I -rich parts [85].

Figure 4.27c shows the contour lines of $\Delta C = C_V - C_I$ at 1000°C using the intrinsic point defect parameters of Nakamura [43] in Table 4.1. When the contour lines of Fig. 4.27c and the defect distribution of Fig. 4.27b are compared, the shapes of the contour line of ΔC agree well with the boundary lines for the defect regions. This shows that ΔC can be used to define the domain in which each type of defect is generated.

Figure 4.28b shows an X-ray topograph made using specimens cut along the axis of another crystal grown with a changing pulling rate as shown in Fig. 4.28a, and subjected to a two-step thermal anneal to precipitate the interstitial oxygen. The position of the OSF ring is again clearly changed by the pulling rate. Usually, the difference between the concentration of vacancies and self-interstitials has

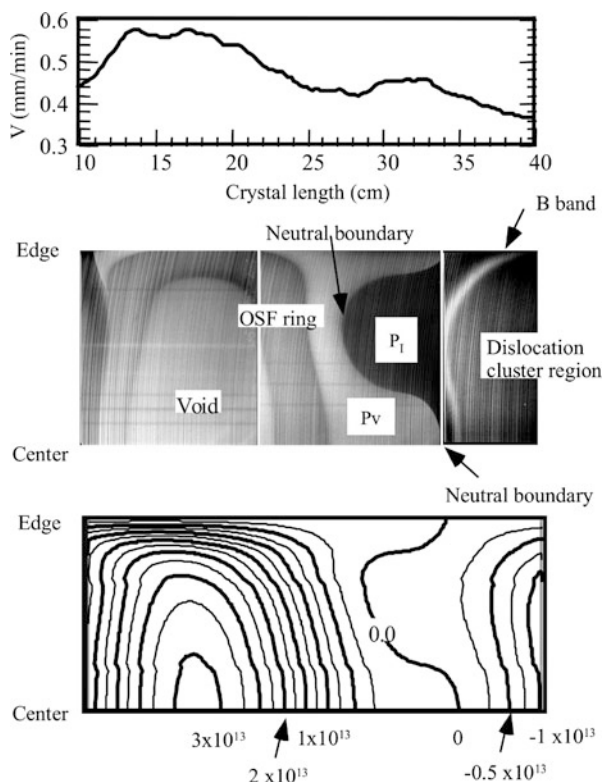


Fig. 4.27 Comparison between the defect pattern and the calculated *contour line* of the intrinsic point defect concentration difference. *Top*: Pulling rate over the crystal length. *Middle*: Cross-section X-ray topograph after 2-step annealing. *Bottom*: Calculated contour lines of $\Delta C = C_V - C_I$ at 1000 °C. P_V and P_I are the vacancy-rich and interstitial-rich parts of the crystal, respectively, without grown-in intrinsic point defect clusters. For the calculation only point defect diffusion and pair annihilation are considered as described by Eqs. (4.4), (4.5), (4.6) and (4.7) (Reproduced with permission from [42]. Copyright 2002, The Electrochemical Society)

been used as the criterion for dominant species of point defects [87]. Because the experimental observation shown in Fig. 4.28b is revealing differences in interstitial oxygen precipitation, one needs to take into account the effect of intrinsic point defects on oxygen precipitation for the further interpretation of the observations. This effect can be expressed by the critical oxide precipitate radius r_c [64, 67]

$$r_c \approx \frac{2\sigma}{\frac{xk_B T}{\Omega_{SiO_x}} \ln \frac{C_{O_i}}{C_{O_i}^*} \left(\frac{C_V}{C_V^*} \right)^\beta \left(\frac{C_I^*}{C_I} \right)^\gamma}, \quad (4.15)$$

with σ the interface energy between SiO_x and Si and Ω_{SiO_x} the molecular volume of the oxide phase that is formed, e.g. amorphous SiO_2 or SiO . k_B is the

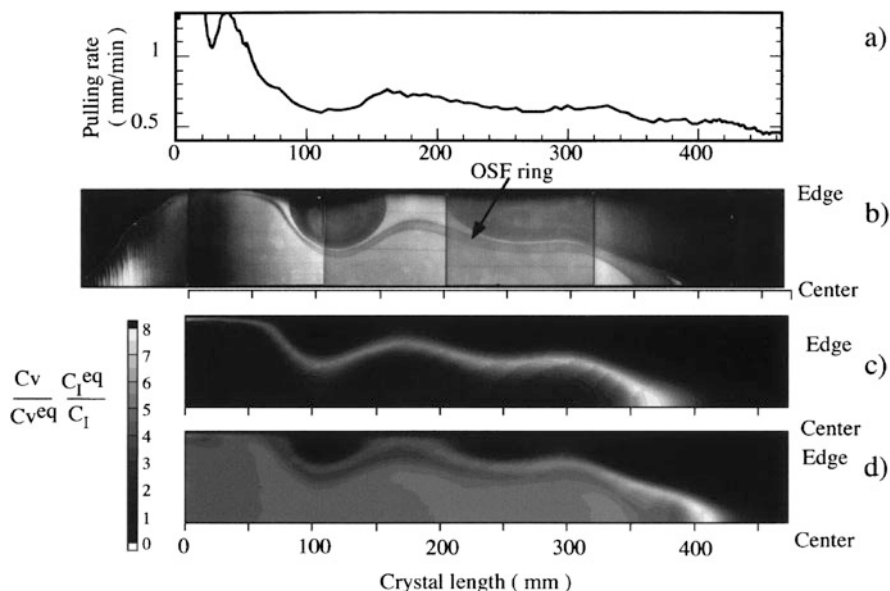


Fig. 4.28 (a) Change of pulling rate. (b) X-ray topograph made using specimens cut along the axis of crystals grown with the change of pulling rate shown in (a) and subjected to the two-step anneal. (c) and (d) Calculated maps of the ratio of the supersaturation of vacancies over the supersaturation of self-interstitials when each crystal position passes the position at 950 and 700 °C, respectively (Reprinted from [38], Copyright 2000, with permission from Elsevier). Besides point defect diffusion and pair annihilation as described by Eqs. (4.4), (4.5), (4.6) and (4.7), also the formation and growth of vacancy clusters is taken into account in this calculation. The model includes the absorption of intrinsic point defects by voids

Boltzmann constant. C_V , C_V^* , C_I , C_I^* and C_{O_i} , $C_{O_i}^*$ are the actual and the thermal equilibrium concentrations of vacancies V , self-interstitials I and interstitial oxygen O_i , respectively. β and γ are the number of vacancies and interstitials, respectively, that are absorbed per precipitating oxygen atom.

This equation describes the relationship between the critical radius of oxide precipitates and the point defect concentrations when the strain is assumed to be entirely released by the intrinsic point defect emission or absorption. It describes how the increase of the ratio of supersaturation of $(C_V/C_V^eq)(C_I^eq/C_I)$ decreases the critical radius of oxide precipitates and thus enhances oxygen precipitation. Therefore, in the following, the ratio $(C_V/C_V^eq)(C_I^eq/C_I)$ is used as the criterion instead of $(C_V - C_I)$ [53] or $(C_V - C_V^eq) - (C_I - C_I^eq)$ [14].

Figure 4.28c shows the calculated map of $(C_V/C_V^eq)(C_I^eq/C_I)$ when each crystal position passes the position at 950 °C. As shown, the peak position of $(C_V/C_V^eq)(C_I^eq/C_I)$ corresponds with the position of the OSF ring. Because the oxide precipitates leading to the formation of the stacking faults in the OSF ring are formed in the temperature range between 900 and 1000 °C [24] during the crystal

pulling process, formation of the OSF ring is assumed to be caused by the strong supersaturation of vacancies at 950 °C.

The peak of $(C_V/C_V^{eq})(C_I^{eq}/C_I)$ forms via the following process. The vacancy concentration at the center of the crystal is always higher than at the periphery side due to the dependence of G on the radial position. Therefore, the vacancy clusters in the central part begin to form earlier, and the vacancy concentration decreases with the absorption of vacancies by the vacancy clusters. Due to that the vacancy concentration becomes lower in the center than at the periphery where the vacancy clusters did not yet form. As a result, the peak of vacancy supersaturation forms just after the void formation in the central part of the crystal. Calculations allowed to reproduce OSF ring formation based on the the proposal of Harada et al. [21] that large grown-in oxide precipitates form the nuclei for the stacking faults leading to the OSF ring.

Figure 4.28d shows the calculated map of $(C_V/C_V^{eq})(C_I^{eq}/C_I)$ when each crystal position passes the position at 700 °C. As shown, the distribution of $(C_V/C_V^{eq})(C_I^{eq}/C_I)$ at 700 °C corresponds well with the distribution of oxygen precipitates formed by the two step annealing. Assuming that the nuclei that grow to full precipitates by annealing below 1000 °C are formed in the temperature range between 600 and 750 °C during the crystal growth process, the distribution of oxygen precipitation corresponds well with the intrinsic point defect supersaturation ratio at 700 °C.

Although it has been assumed by most researchers that the precipitated phase is SiO_2 and most precipitation simulators are based on that assumption, there is more and more evidence that the precipitated phase is SiO_x with x close to 1 [10, 45, 54, 65, 70] which will have a significant influence on the critical precipitate size given by (4.15) and thus on the BMD density which might change the results shown in Fig. 4.28c, d unless also the intrinsic point defect parameters are adapted.

From these figures one can define different zones in the crystal according to the value of $\Delta C = C_V - C_I$:

Vacancy-rich

- Void region: $>1.5 \times 10^{13} \text{ cm}^{-3}$
- OSF region: $1.5 \times 10^{13} - 0.5 \times 10^{13} \text{ cm}^{-3}$
- Defect-free region (PV): $0 - 0.5 \times 10^{13} \text{ cm}^{-3}$

Interstitial-rich

- Defect-free region (PI): $0 \text{ to } -0.25 \times 10^{13} \text{ cm}^{-3}$
- I type defect region: $< -0.25 \times 10^{13} \text{ cm}^{-3}$

Since this result is obtained by fitting only one growth condition, one needs to verify whether or not this criterion of ΔC calculated using this parameter set also holds for other growth conditions. To verify this, the growth rates at which the defect types changed were investigated using 200 mm diameter crystals grown under 14 different growth conditions. V_{osf} , the pulling rate at which the OSF ring closes, $V_{neutral}$, the pulling rate at which the intrinsic point defects become neutral and do

not cluster, and V_{id} , the pulling rate at which the self-interstitial type defects appear, were investigated in particular. These pulling rates were investigated at the center of the crystal and at 90 mm from the center. Calculations were performed using the temperature distributions calculated by a global heat transfer analysis method that took into account melt convection and the actual shapes of the crystal-melt interface. In Fig. 4.29a, b, the horizontal axis shows the values of V_{osf} , $V_{neutral}$, and

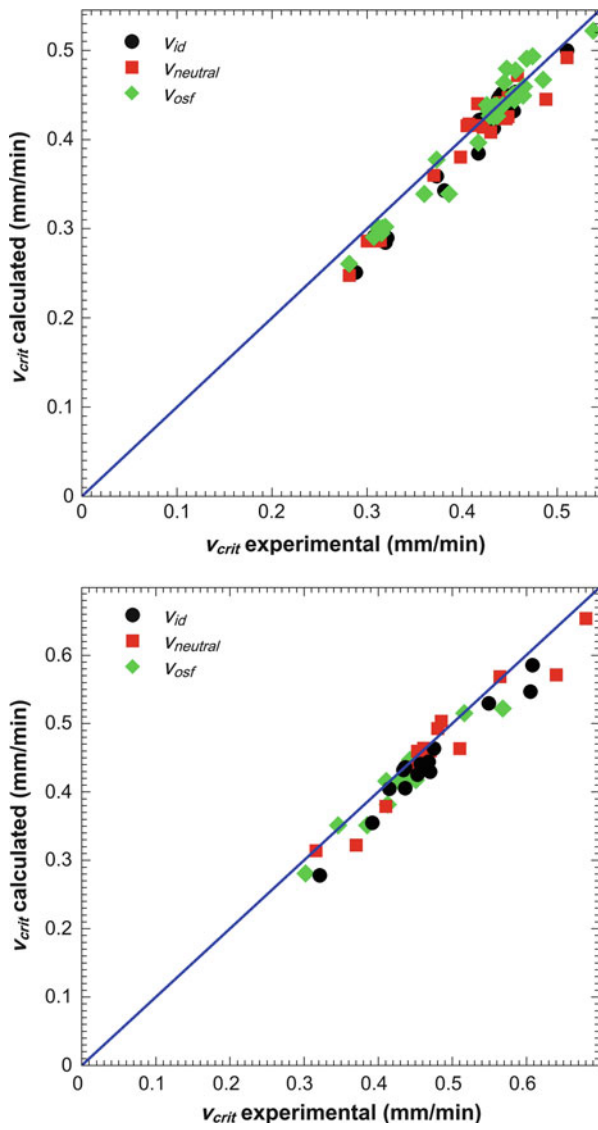


Fig. 4.29 Comparison between experimental and predicted values of V_{osf} , $V_{neutral}$, and V_{id} [42].
Top: Crystal center. *Bottom:* 90 mm from the crystal center

V_{id} obtained experimentally, while the vertical axis shows the values predicted by calculation. The criterion of ΔC calculated using the Nakamura et al. parameter set corresponds well to the experimental result.

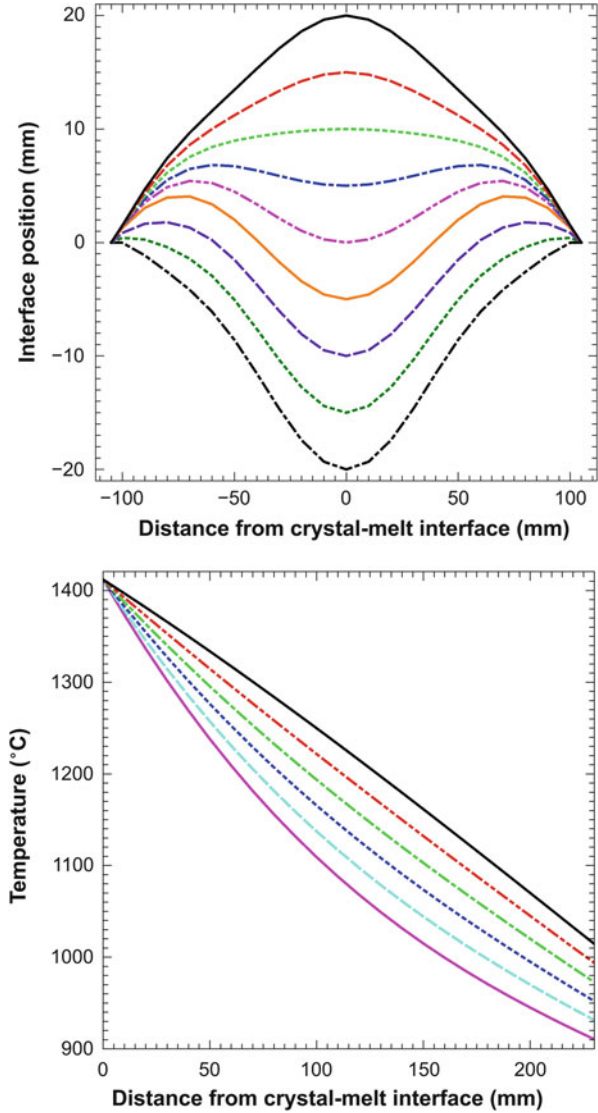
4.5 Optimum Condition for a Grown-in Defect Free Intrinsic Crystal

Using the intrinsic point defect parameters of Nakamura et al. [43] in Table 4.1, the growth condition whereby the concentrations of intrinsic point defects are such that all positions in the radial direction are free from grown-in defects, was examined. In other words, the condition at which ΔC falls in the range between -0.25×10^{13} and $0.5 \times 10^{13} \text{ cm}^{-3}$ at all positions in the radial direction, was examined. This state is obtained for the crystal length between 26 and 34 cm as shown in Fig. 4.27. The temperature distribution at the crystal periphery and the shape of crystal-melt interface determine the temperature gradient (G) inside the crystal. Therefore, the growth conditions that determine the distribution of the intrinsic point defect distribution are: (1) the temperature distribution at the crystal periphery, (2) the shape of the crystal-melt interface, and (3) the growth rate. Using typical data of 200 mm-diameter crystals, a series of crystal-melt interface shapes (Fig. 4.30a) was established (a) as well as axial-temperature distributions at the crystal periphery (Fig. 4.30b). Subsequently the relationship between v and the radial distribution of ΔC was calculated using combinations of both sets of data.

Figure 4.31 illustrates the change of the formation boundary of the self-interstitial type defects ($\Delta C = -0.25 \times 10^{13} \text{ cm}^{-3}$) and OSF ($\Delta C = 0.5 - 1.5 \times 10^{13} \text{ cm}^{-3}$) and of the voids ($\Delta C > 1.5 \times 10^{13} \text{ cm}^{-3}$) by the crystal growth rate. The temperature gradients of the crystal peripheries (G_{outer}) in Fig. 4.31 are 3 K/mm near the melting point and the height differences of the center and periphery of the crystal-melt interface ($H = H_{center} - H_{outer}$) are -15 mm (left figure) and +15 mm (right figure), respectively. In this way a growth rate was obtained at which all radial positions become defect-free (right figure) and wafers without grown-in defects can be produced from a crystal grown within that growth rate range. In the right figure, the tolerance (Δv) of the growth rate in order to obtain a grown-in-defect-free crystal is only 0.02 mm/min. Such growth rate window could not be obtained for the left figure and one of the defect types will always be found at some position in the radial direction.

The tolerance (Δv) of the growth rate to obtain a grown-in-defect-free crystal with all combinations of G_{outer} and H was examined and the results are summarized in Fig. 4.30. Figure 4.32 shows the contour lines of Δv for G_{outer} and H . As the figure shows, a grown-in-defect-free crystal (positive Δv) can be found in a specific region for G_{outer} and H . The explanation for this is relatively straightforward. According to heat transfer analysis, an increase of G_{outer} increases the ratio of G_{outer}/G_{center} with G_{center} the temperature gradient at the crystal center, hence the

Fig. 4.30 Series of the shapes of the crystal-melt interface (*top*) and axial-temperature distributions at the crystal periphery used in the calculations (*bottom*) [42]. All values are derived from typical data for 200 mm diameter crystals. G at the crystal periphery (G_{outer}) is the temperature gradient from melting point to 1350 °C. G_{outer} varies between 1.5 and 4.5 K/mm. The height at the crystal center (H) is -20 to $+20$ mm



distribution of G becomes non-uniform in the radial direction. The increase of H , meanwhile, increases G_{center} , hence the distribution of G in the radial direction is made uniform by the increase of H under a condition with a higher G_{outer} . To obtain a near neutral state of point defects in all positions in the radial direction, the distribution of G (in other words, v/G) in the radial direction must be uniform. Therefore, G_{outer} in the region free of grown in defects is dependent on H , as shown in Fig. 4.32.

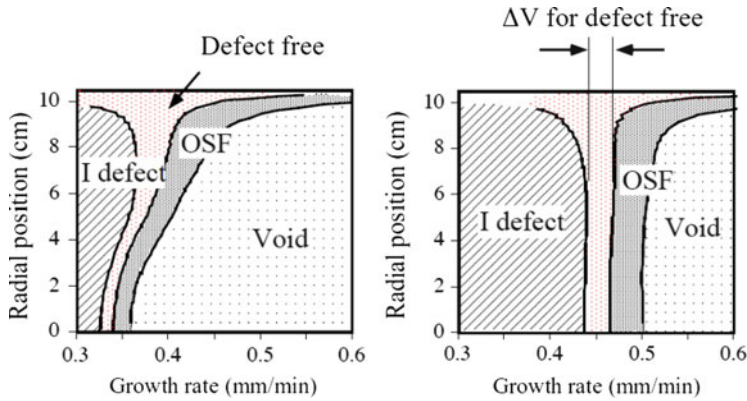


Fig. 4.31 Change in the formation boundary of the self-interstitial type defect ($\Delta C = -0.25 \times 10^{13} \text{ cm}^{-3}$) and OSF ($\Delta C = 0.5 \times 10^{13} - 1.5 \times 10^{13} \text{ cm}^{-3}$) by the growth rates. $G_{\text{outer}} = 3 \text{ K/mm}$, *left*: $H = -15 \text{ mm}$, *right*: $H = +15 \text{ mm}$ (Reproduced with permission from [42]. Copyright 2002, The Electrochemical Society)

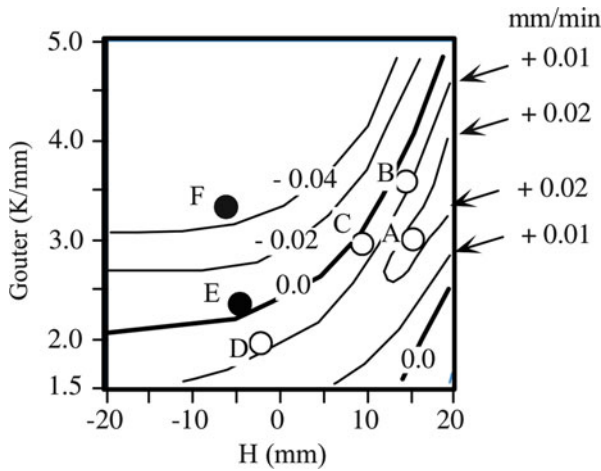


Fig. 4.32 Contour line of Δv (mm/min) for G_{outer} and H . Δv is the tolerance of the growth rate for the grown-in-defect-free state. Negative Δv indicates that the defect-free state does not exist (Reproduced with permission from [42]. Copyright 2002, The Electrochemical Society)

Table 4.2 Δv for the conditions of the plots shown in Fig. 4.32

	G_{outer} (K/mm)	H (mm)	Δv (mm/min)
A	3.3	15.0	0.020
B	3.5	14.0	0.009
C	3.0	9.3	0.002
D	1.9	−2.5	0.005
E	2.2	−5.0	−0.002
F	3.3	−6.0	−0.040

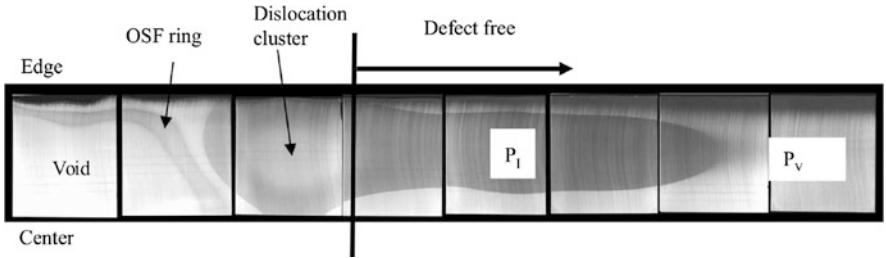


Fig. 4.33 Cross-sectional X-ray topographs of a grown-in-defect-free 200 mm diameter Si crystal after the 2-step annealing [37]. The interstitial oxygen concentration is about 1.4×10^{18} (atoms/cm³, old ASTM). P_V : Vacancy rich grown-in-defect-free crystal, P_I : Interstitial rich grown-in-defect-free crystal

To verify Fig. 4.32, experiments were performed similar to those shown in Fig. 4.27 and evaluated Δv for each growth condition. Table 4.2 shows Δv for the conditions of the plots shown in Fig. 4.32. The calculation results correspond well to the experimental results. Figure 4.33 shows the example of a grown-in-defect-free crystal grown under the condition D in Fig. 4.32.

From Fig. 4.32, the maximum of tolerance (Δv) of the growth rate for the grown-in-defect-free state is around 0.02 mm/min. Thus, the following three problems must be solved in order to be able to obtain crystals free of grown-in defects requiring a tight control of the crystal pulling conditions to have a high yield production:

- High-precision control of the growth rate, $\pm 1\text{--}3\%$.
- Reproducibility of G , $\pm 1\text{--}3\%$.
- The control of the growth rate depends on the crystal length (G_{outer} and the shape of the crystal-melt interface change in crystals of different lengths).

4.6 Impact of Stress on v/G

Recently, Vanhellemont [66] predicted that the effect of thermal stress on the equilibrium concentrations of point defects significantly changes $[v/G]_{crit}$. Nakamura et al. [44] were the first to report experimental results for 300 mm diameter crystals clearly showing that compressive thermal stress increases the incorporated vacancy

concentration and reduces $[v/G]_{crit}$. Using the same experimental data it was shown that one should take into account that previously determined intrinsic point defect parameters that were used are “contaminated” by not taking into account the effect of stress to explaining the experimental observation on grown-in intrinsic point defect clusters. This “built-in” stress effect can be taken into account to some extent by fitting the experimental data using a stress dependent Voronkov criterion yielding a consistent estimate of the pre-factors of the exponential equations describing the diffusivity and thermal equilibrium concentration of the intrinsic point defects [78]. Subsequently it was shown that when assuming plane stress, the experimental data of Nakamura et al. can be reproduced accurately using the ab initio calculated impact of plane stress on the intrinsic point defect formation energies [56]. It is interesting to remark also that an arbitrary linear fit lies very close the best fit using ab initio formation energies obtained for plane stress as is illustrated in Fig. 4.34. The linear fit using all data points yields [79]

$$[v/G]_{crit} = (0.1720 \pm 0.0007) + (0.00146 \pm 0.00007)\sigma_{ave}, \quad (4.16)$$

with $[v/G]_{crit}$ in $\text{mm}^2 \text{K}^{-1} \text{min}^{-1}$ and the average plane stress σ_{ave} in MPa. The goodness of fit R^2 is 0.844.

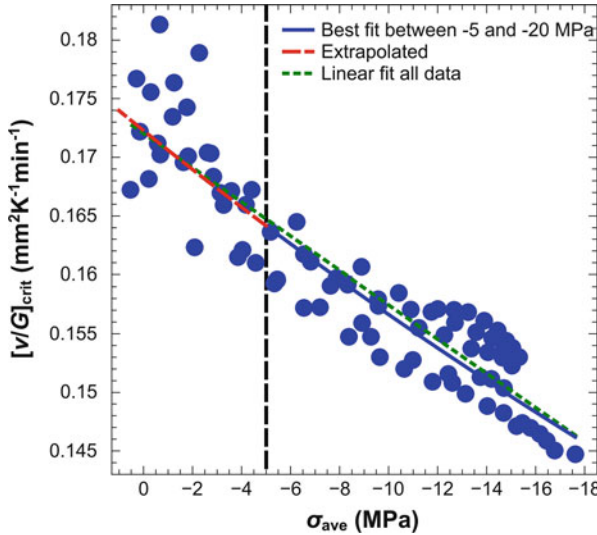


Fig. 4.34 Γ_{crit} as function of planar stress at the crystal-melt interface fitted to experimental data for 300 mm diameter CZ silicon crystals, using the data and point defect parameters of Nakamura et al. [43]. The fit was performed for average planar stresses between -5 and 20 MPa, and suggests that the intrinsic point defect data of Table 4.1 were obtained for an average stress level of -5.1 MPa. A linear fit using all data points, lies very close [79]

When the crystal diameter is 300 or 450 mm and the shape of crystal-melt interface is concave (center position is higher than that of periphery), the thermal stress is thus high enough to affect significantly $[v/G]_{crit}$. In this case, the thermal stress at the center of crystal-melt interface is compressive and that at the periphery is much lower and close to zero. Therefore, a homogeneous distribution of G to the radial direction is not appropriate any more to grow a grown-in-defect-free crystal and it is necessary to modify the G distribution for the compensation of the mentioned stress effect.

The described impact of the thermal stress on $[v/G]_{crit}$ will thus become a critical issue in the development of 450 mm diameter Si crystal pulling processes and will also pose a serious challenge for surface inspection tools based on light scattering as small voids can be formed inside nominal “COP-free” regions due to compressive stress variations [27].

4.7 Impact of Doping: Dopant Induced Stress and Trapping

4.7.1 Reported Experimental Observations

The impact of doping on intrinsic point defect cluster formation during single-crystal silicon growth was already realized in the early days and possible mechanisms to explain this impact were already identified, i.e. change of Fermi level, dopant atom size related stress, dopant atoms acting as traps for intrinsic point defects and complex formation of intrinsic point defects with dopant atoms [6, 11, 12]. Transmission electron microscopy investigations revealed e.g. small self-interstitial type dislocation clusters in $3 \times 10^{18} \text{ B cm}^{-3}$ doped CZ samples while in $1.2 \times 10^{18} \text{ Sb cm}^{-3}$ doped samples only vacancy type inclusions were observed, most probably the first direct observation of voids formed by vacancy clustering during crystal growth [11]. Main conclusions of that work were that for CZ-grown crystals, the formation of self-interstitial clusters was suppressed by doping with donors (Sb, P and As) while doping with acceptors (B, Ga) suppresses formation of vacancy clusters whereby the dopant concentrations should at least 10^{17} cm^{-3} to have a noticeable effect [12]. In addition to the effect of electrically active dopants, As shown in Figs. 4.35 and 4.36, Abe et al. [2, 6] also studied the effect of various dopants on grown-in defects in FZ crystals. A strong suppression of vacancy type point defect clusters was e.g. observed in case of N and C doping while O doping led to an increase of the vacancy cluster formation.

4.7.1.1 Impact of Dopants

The impact of B doping of COP distribution was studied and results are shown in Figs. 4.37 and 4.38. Heavy B doping makes the crystal more interstitial rich than a

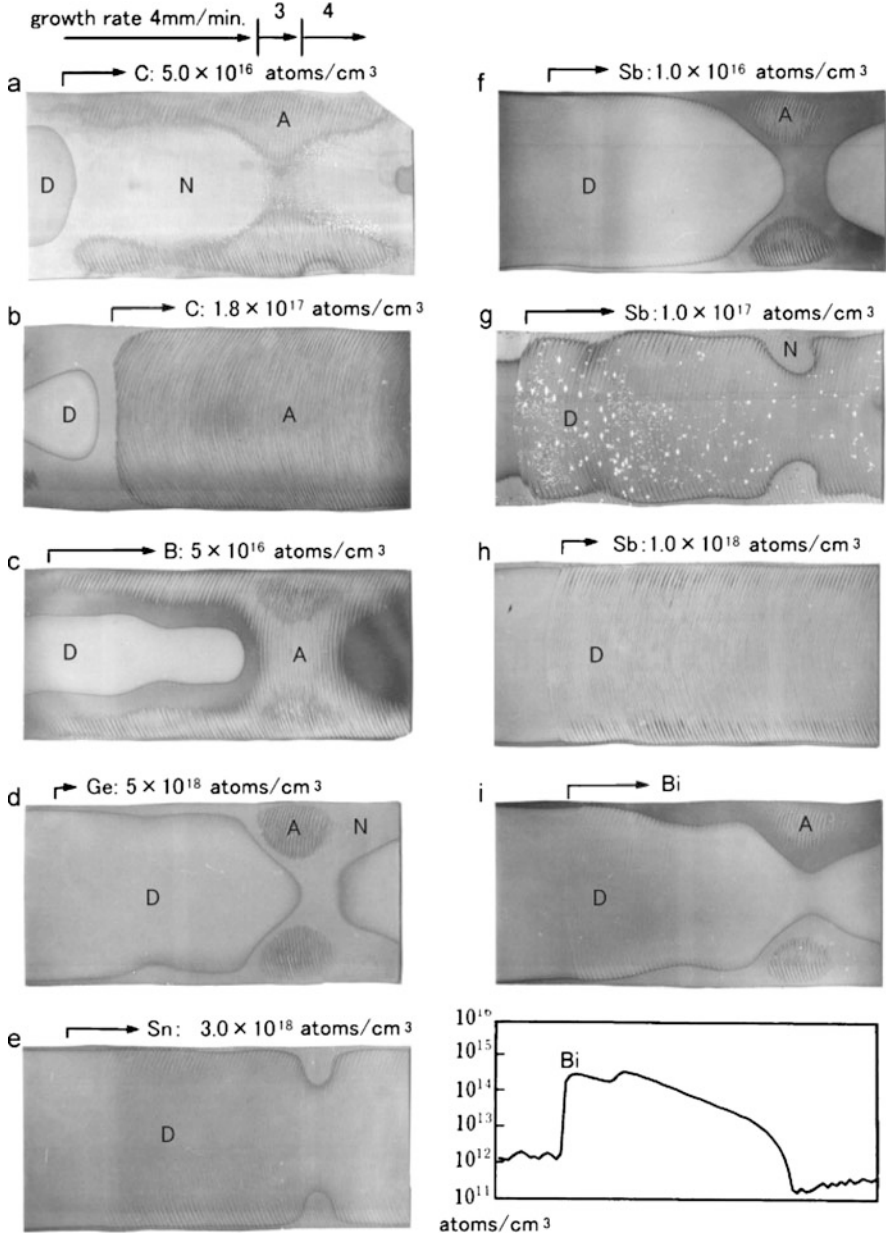


Fig. 4.35 X-ray topographs of longitudinally cut wafers after Cu decoration of 42 mm FZ crystals doped with different impurities (Reprinted from [2], Copyright 2011, with permission from Elsevier). Two different C concentrations (a) and (b), B (c), Ge (d), Sn (e), three different Sb concentrations (f), (g) and (h), and Bi with concentration profile (i)

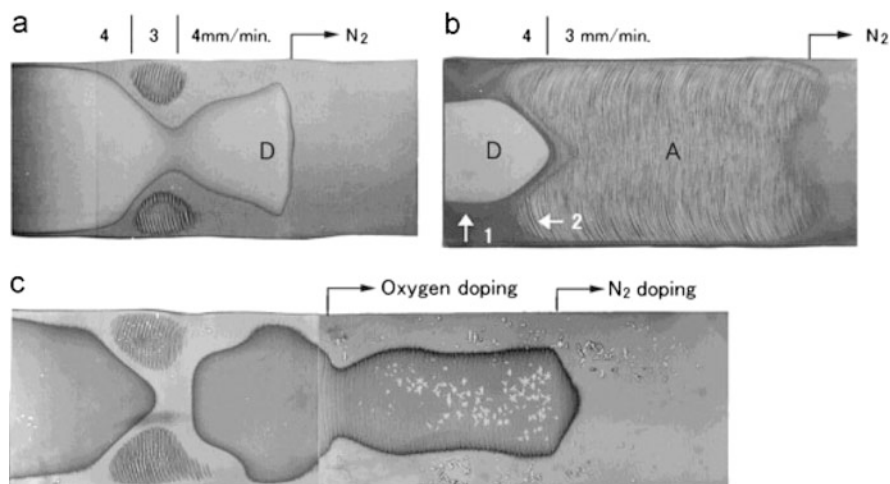


Fig. 4.36 X-ray topographs of FZ specimens after Cu decoration (Reprinted from [2], Copyright 2011, with permission from Elsevier). *Top left*: Generation of D-defects and *top right*: A-defects is suppressed by N doping. *Bottom*: The effect of O and N doping on D-defect formation

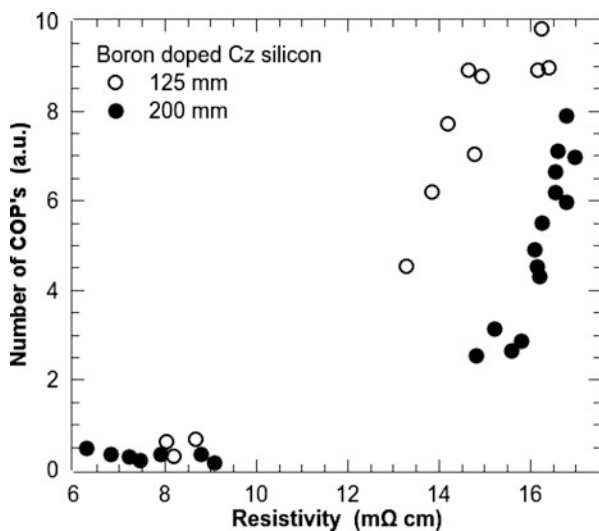


Fig. 4.37 Number of COP's after 4h SC1 in 125 and 200 mm boron doped CZ Si crystals [68]

moderately one for the same v/G . This leads to a decrease of the COP density with ultimately the disappearance of COP's. As illustrated in Fig. 4.38 the OSF ring also moves inwards with increasing B concentration confirming that the crystal gradually changes from vacancy-rich to interstitial-rich.

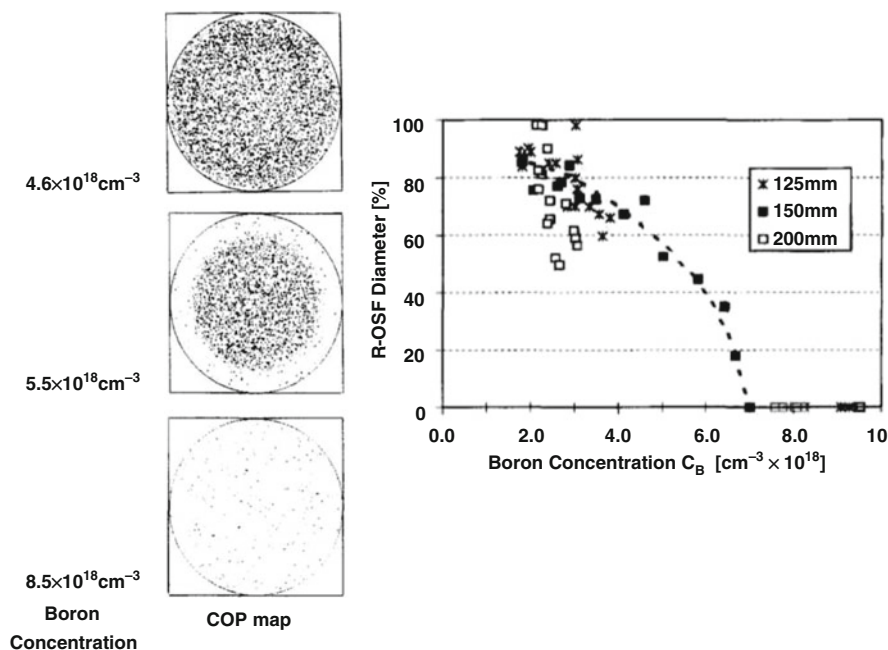
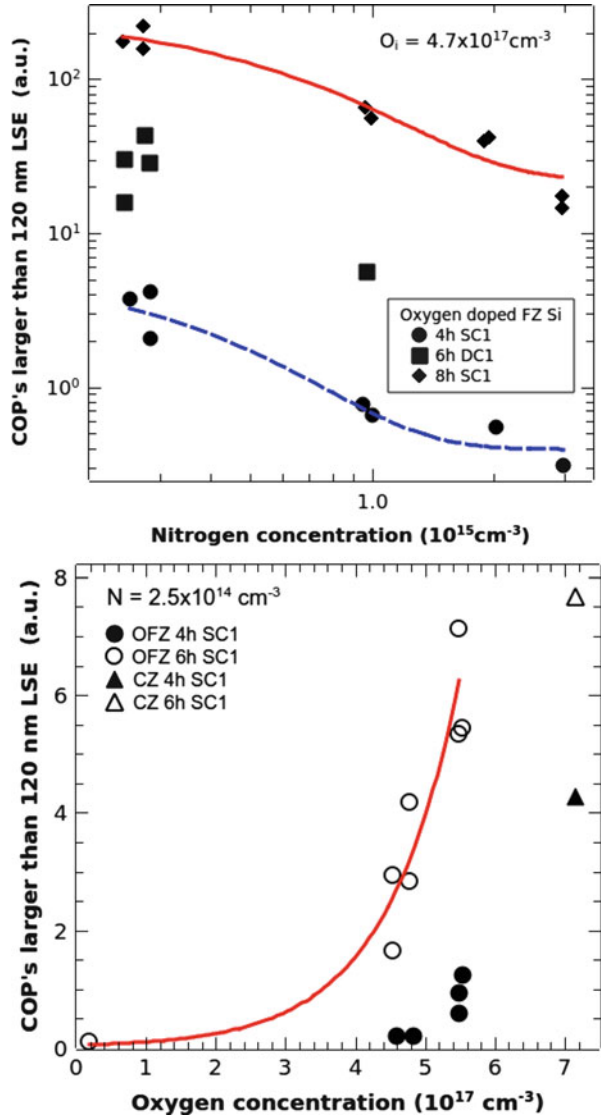


Fig. 4.38 *Top*: Radial COP distribution on wafers prepared from 150 mm diameter Si crystals pulled with similar v/G but with different boron concentration C_B . *Bottom*: OSF-ring diameter as function of C_B for 125, 150 and 200 mm crystals (Reprinted from [15], Copyright 1997, with permission from Elsevier)

A similar effect on COP's is observed when doping with nitrogen as illustrated in Fig. 4.39. The bottom figure shows results obtained on oxygen doped FZ Si illustrating that the presence of interstitial oxygen is needed in order to form COP's that are large enough to be observed. Both results are in agreement with the X-ray topography observations on nitrogen doped FZ as shown in Fig. 4.36.

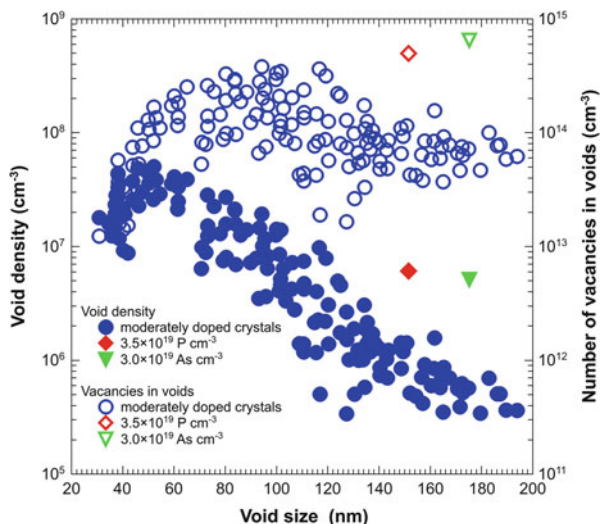
Dornberger et al. [15] reported a linear dependence of Γ_{crit} on active boron concentration based on the study of the dependence of the stacking fault ring position on the level of boron doping. Similar results were obtained by Valek et al. [63]. Nakamura et al. [43] published results of an extensive study of the effect of seven impurities, i.e. B, C, O, N, Sb, P and As, on grown-in defects in CZ-grown silicon crystals, discussing also the different mechanisms mentioned above. They concluded that doping with high concentrations of acceptors or donors (e.g. about $5 \times 10^{18} \text{ cm}^{-3}$ B and about $5 \times 10^{19} \text{ cm}^{-3}$ As and P) leads to a significant change of the intrinsic point defect equilibrium concentrations and thus also to significant changes of Γ_{crit} whereby acceptor doping makes the crystal more self-interstitial-rich, while donor doping leads to a more vacancy-rich crystal. At the same time, the impurities that enhance the incorporation of one type of intrinsic point defect also suppress partially the clustering of these point defects into grown-in defects

Fig. 4.39 The number of COP's larger than 120 nm LSE, as function of the nitrogen (*top*) and oxygen (*bottom*) concentration in 125 mm diameter, oxygen doped FZ and CZ crystals [20, 68]. The lines are empirical fits with an exponential function to guide the eye



when the impurities strongly bind with the intrinsic point defects. This is the case for N, P and As which are dopants that enhance vacancy incorporation as evidenced by the shift of the OSF ring position but at the same time suppress void formation [41]. This is illustrated for P and As doping in Fig. 4.40. B and C doping, on the other hand enhance self-interstitial incorporation [15] but suppress the formation of dislocation clusters [7].

Fig. 4.40 Void density vs. void size for moderately doped CZ Si crystals and for a heavily P doped and a heavily B doped CZ Si crystal [43]. An estimate of the total vacancy concentration incorporated in the voids, assumed to be octahedral, is also shown



4.7.2 *Ab Initio* Calculation of Dopant Impact on Uncharged Intrinsic Point Defects

4.7.2.1 Calculation Details

The formation energies of uncharged V and I at all sites within a sphere with 0.6 nm radius around the dopant atom for V and with 0.5 nm radius for I are calculated by DFT. Substitutional p-type (B and Ga), neutral (C, Ge, and Sn) and n-type (P, As, Sb, and Bi) dopants were considered.

The formation energy of V within a sphere with 0.6 nm radius around the dopant atom is calculated as follows. The cell size of a perfect 216-atom supercell after its geometry is optimized, is 1.6392 nm. A dopant atom is introduced at the center of perfect 216-atom supercells and a vacancy is placed at the 1st to 5th neighbors from the dopant atom. It turns out that there are 46 possible sites for V within the 0.6 nm radius sphere around the dopant atom. The formation energy of V at each site is calculated by fully relaxing the ionic coordinates. The number of sites at 1st to 5th neighbors from the dopant atom are 4 (1st), 12 (2nd), 12 (3rd), 6 (4th) and 12 (5th), respectively.

The formation energy of I within a sphere with 0.5 nm radius around the dopant atom is calculated as follows. A self-interstitial I is placed at all interstitial sites around the dopant atom. Hereby I at the tetrahedral (T)-, hexagonal (H)-, [110] dumbbell (D)-, [100] D-, and [114] D-sites is considered as shown in Fig. 4.41. The formation energy for each site is calculated by fully relaxing the ionic coordinates. Further details on the calculation procedures can be found in [55].

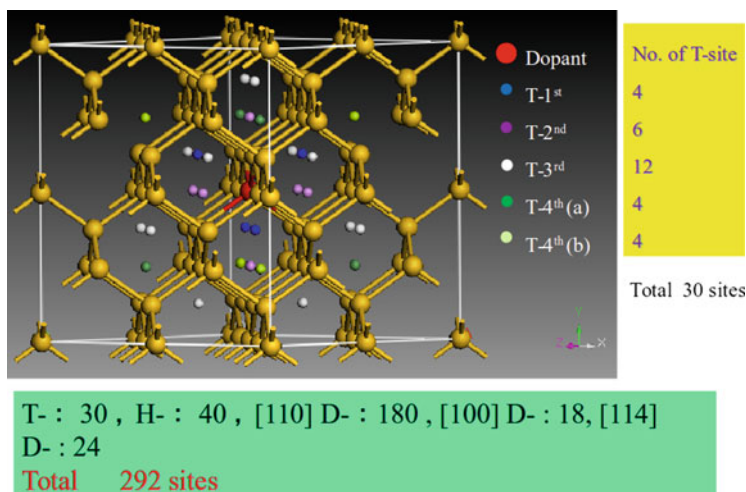


Fig. 4.41 Possible sites of a vacancy within a sphere with 0.6 nm radius around dopant atom (*red atom*) in a 64-atom supercell [55]

4.7.2.2 Intrinsic Point Defect Formation Energy

As an illustration, Fig. 4.42 shows the calculated vacancy formation energy as function distance from common neutral and n-type dopant atoms. The dotted lines from the 1st to the 5th position in the figure indicate the distance from the dopant before the cell size and ionic coordinates are relaxed. It is clear that $E_{V,dope}^f$ at the 1st site differs for the different dopants. The formation energy of vacancies with larger dopants is smaller than with smaller dopants. Since the electrical state is almost the same for the same types of dopants, this result is mainly due to the difference in local strain. Furthermore, $E_{V,dope}^f$ at and far from the 2nd sites are close for neutral dopants without changing the electrical state, and close to that in undoped Si. This indicates that local strain effects are only important at the 1st site from the dopant atom. The type and magnitude of local strain differ for the n-type dopants P, As, Sb, and Bi. However, starting from the 2nd site, $E_{V,dope}^f$ is nearly the same for all n-type dopants and about 0.3–0.4 eV lower than that in perfect Si. This illustrates that not local strain but the electrical state around n-type dopants mainly determines the V formation energy.

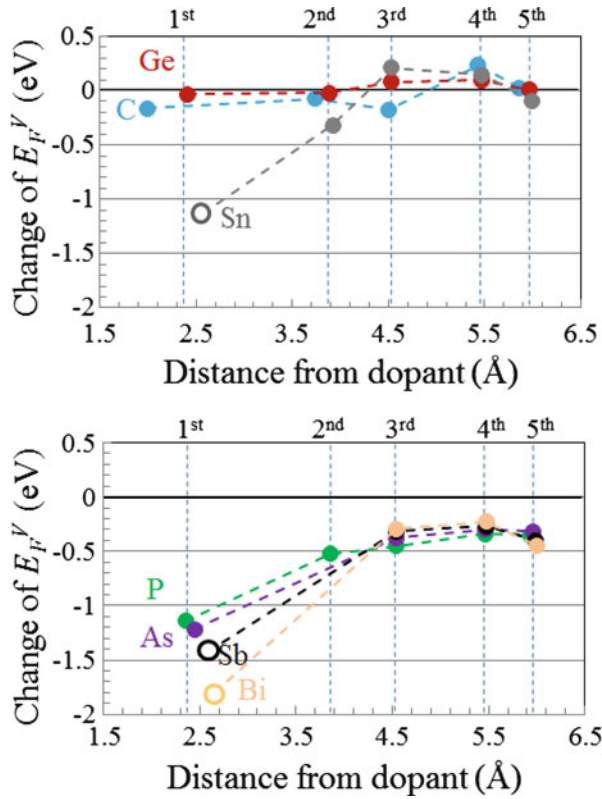


Fig. 4.42 *Top:* Dependence of the change of vacancy formation energy from that for Jahn-Teller distortion in a perfect Si crystal on the distance from neutral and *bottom:* n-type dopant atoms. *Open circles* for Sn, Sb, and Bi indicate split vacancies. *Dotted lines* from 1st to 5th indicate the distance from the dopant before cell size and ionic coordinates are relaxed (Reprinted with permission from [55]. Copyright 2013, AIP Publishing LLC)

More results for $E_{V,dope}^f$ in case of p-type dopants and also similar results for the formation energy $E_{I,dope}^f$ of the self-interstitial in case of neutral-, n- and p-type dopants, can be found elsewhere [55].

The DFT calculations also allow to calculate $C_V - C_I$ as function of dopant concentration and type and thus give an indication when a crystal changes from vacancy-rich to self-interstitial-rich as illustrated in Fig. 4.43 for common dopants in Si [55]. Excellent agreement between calculation and experiment is obtained.

- Top graph of Fig. 4.43:
 - $Sb > 10^{17} \text{ cm}^{-3}$. D-defects increase;
 - $Sb = 1 \times 10^{18} \text{ cm}^{-3}$, $Sn = 3 \times 10^{18} \text{ cm}^{-3}$. Similar impact on D-defects increase;
 - $Bi = 10^{15} \text{ cm}^{-3}$. No impact on D-defects [2].

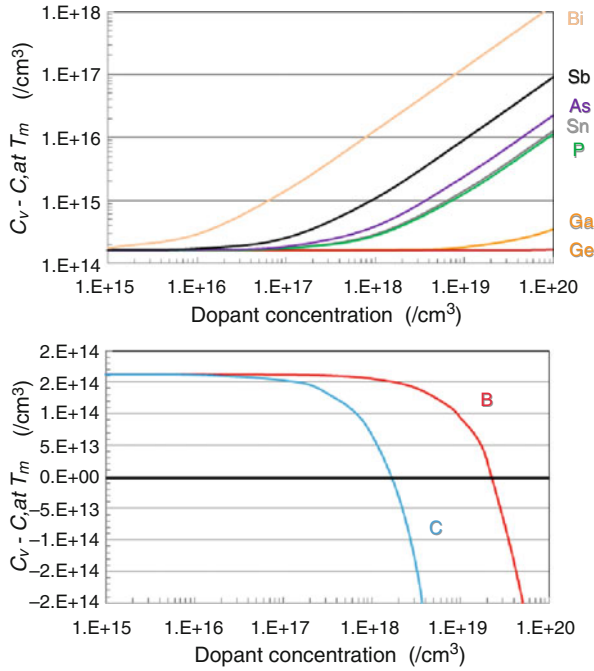


Fig. 4.43 Calculated dependence of $C_V - C_I$ at melting temperature of Si on dopant concentration and type. The parameters of Table 4.1 were used for the calculation. Excellent agreement between calculation and experiment is obtained (Reprinted with permission from [55]. Copyright 2013, AIP Publishing LLC)

- As $> 2 \times 10^{18} \text{ cm}^{-3}$. Voids increase [57].
- Ge $= 10^{20} \text{ cm}^{-3}$. No impact on voids [76].
- Bottom figure of Fig. 4.43:
 - B $> 5 \times 10^{18} \text{ cm}^{-3}$. OSF-ring shrinks [15].
 - B $= 2 \times 10^{19} \text{ cm}^{-3}$. I-rich crystal;
 - C $= 6 \times 10^{16} \text{ cm}^{-3}$. V decreases [43].

One could summarize the results of dopant effects as follows: Self-interstitials for p-type dopants are rather stable at T-sites, while self-interstitials for neutral and n-type dopants are rather stable at D-sites. Furthermore, $E_{I,dope}^f$ differs for the types of dopants as follows:

- In case of p-type dopants, $E_{I,dope}^f$ at T-sites up to $\approx 0.6 \text{ nm}$ is reduced by about 0.5–1.3 eV compared to that in perfect Si. No remarkable differences in $E_{I,dope}^f$ are obtained for B and Ga atoms. These results are due to the Coulomb (long-range) interaction between acceptor and positively charged I at the T-site.

- In case of neutral dopants, $E_{I,dope}^f$ at the D-sites up to ≈ 0.3 nm from C atom is reduced by about ≈ 0.7 – 1.3 eV compared to that in perfect Si while Ge and Sn atoms have no impact on $E_{I,dope}^f$. These results are due to the larger local tensile strain introduced by the C atom, which reduces the formation energy of the neutral I at the D-site. In case of n-type dopants, $E_{I,dope}^f$ at the D-sites up to ≈ 0.3 nm is reduced by about 0.5 eV compared to that in perfect Si. P, which gives local tensile strain, shows the largest impact on the neutral I at D-site among the n-type dopants.

Impact of doping on Γ_{crit} . For simplicity it was assumed in case of heavy doping that $C(T_m) = C^{eq}(T_m) = C^{eq,tot}(T_m)$, that E_I^f and E_V^f are the intrinsic values which is a reasonable assumption close to melting temperature and for not too high doping, and that D_I and D_V are not affected by doping.

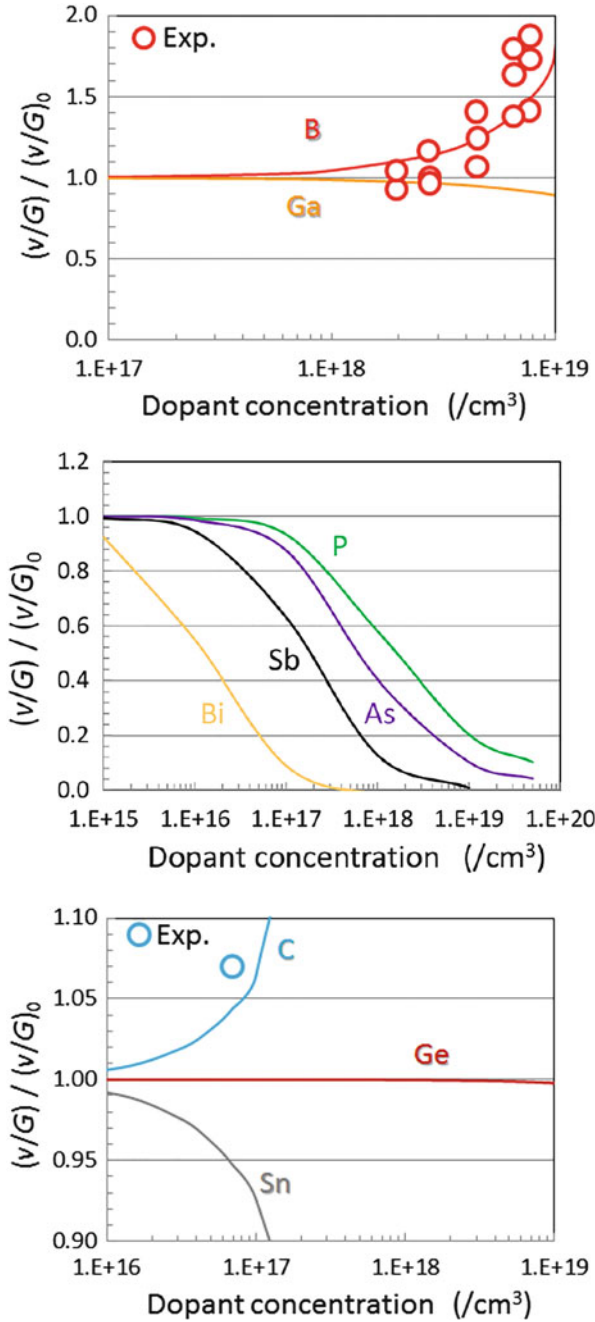
Figure 4.44 shows the calculated dependence on dopant concentration of Γ_{crit} normalized with respect to the intrinsic value Γ_{crit}^0 , assuming zero stress. The circles in the figures for B and C doping are the experimental results obtained by Nakamura et al. [43]. The calculated results for heavy B doping agree well with the experimental results. Although there is only one experimental plot for C doping, it is also close to the calculated line. To the best of our knowledge, no experimental results for the impact of n-type dopants on critical $(v/G)_{crit}$ have yet been reported in literature.

Summarizing the main DFT results: a model was proposed explaining quantitatively the intrinsic point defect behavior in heavily doped Si single-crystals growing from a melt:

- The incorporated total V and I (sum of free V or I and V or I around the dopants) concentration at melting temperature depend on the type and concentration of dopant. This is due to the change in the formation energies of V and I around the dopant atoms, which is caused by the electrical state and magnitude of local strain depending on the types and sizes of the dopant.
- Most of the total V and I concentrations contribute to pair recombination at much higher temperatures than those at which voids are formed (1100°C). This means that the values of $C_V^{eq,tot}(T_m)$ and $C_I^{eq,tot}(T_m)$ determine the impact of the dopant type and concentration on the dominant point defect (with v/G greater than the window of defect free Si) and also the critical $(v/G)_{crit}$.

The main strength of the proposed model is that it explains point defect behavior for all dopants and for all concentrations and is in excellent agreement with all experimental data known to the authors.

Fig. 4.44 Calculated dependence of $(v/G)_{crit}$ on dopant concentration, normalized with respect to the intrinsic value obtained with low doping. The *open symbols* are experimental data (Reprinted with permission from [55]. Copyright 2013, AIP Publishing LLC)



4.8 Open Questions: Impact of Fermi Level and Intrinsic Point Defect Formation Energy Near Crystal-Melt Interface

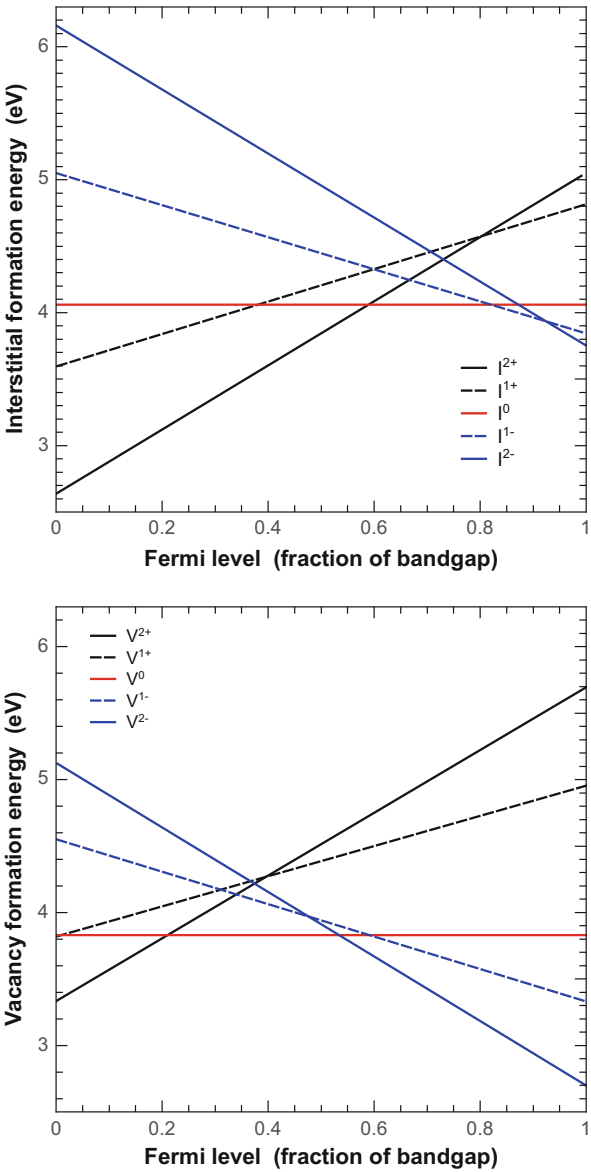
4.8.1 Impact of Fermi Level

Electrically active dopants influence the bandgap and the Fermi level and the bandgap and thus also the formation energy of charged intrinsic point defects as illustrated in Fig. 4.45 (based on DFT calculations at 0 K). In n^+ Si, the double negatively charged vacancy V^{2-} will have the lowest formation energy while in p^+ Si, it is the double positively charged self-interstitial I^{2+} . Close to melting temperature the situation changes as illustrated in Fig. 4.46 and only for very high n-type doping (well above a few times 10^{19} cm^{-3}), V^{2-} still has a slightly lower formation energy than the neutral vacancy V while For p-Si, I^{2+} has the lowest formation energy for all dopant concentrations. Figure 4.47 shows calculated $[v/G]_{crit}$ fitted to experimental data. Fermi level and bandgap effects were thereby taken into account. Figure 4.48 shows the data of Nakamura et al. and Dornberger et al. from the previous figure together with calculated curves showing that the data can be reproduced very well when assuming a different planar thermal stress (= hot zone) for both crystals.

4.8.2 Interstitial and Vacancy Formation Energy Near Crystal Surfaces

$c(4 \times 2)$ structure models of the Si (001) crystal surface were investigated to clarify the behavior of intrinsic point defects near crystal surfaces. Figure 4.49 shows the calculated dependence of the intrinsic point defect formation energy as function of the distance to the (001) surface. Regarding crystal growth from a melt, the most important result is the existence of the formation energy differences between the surface and the bulk for both types of intrinsic point defects. The presence of these energy differences supports the macroscopic model in which the generation and the recombination of Frenkel pairs is more important inside the bulk than at the surface. The obtained results also support that boundary conditions of the point defect concentrations at the surface in simulations can be set at fixed values. Namely, the existence of barriers makes it possible for the surface to act as a reservoir of intrinsic point defects. When simulating crystal growth from a melt, these fixed values for the boundary conditions should, however, be defined, taking into account the impact of the crystal crystal-melt interface.

Fig. 4.45 *Top*: Calculated formation energies for the different charge states of the self-interstitial and *bottom*: the vacancy as a function of the Fermi level expressed as fraction of the bandgap (Reproduced with permission from [77]. Copyright 2013, The Electrochemical Society)



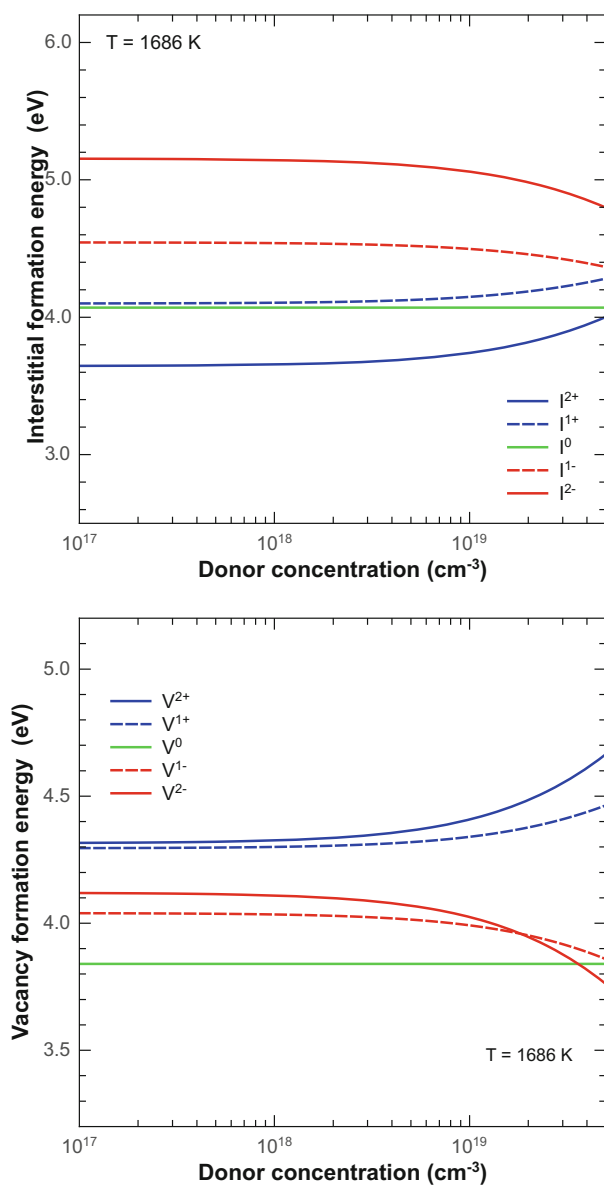


Fig. 4.46 *Top*: Calculated formation energies at 1413°C of the different charge states of the self-interstitial and *bottom*: the vacancy as function of the donor concentration (Reproduced with permission from [77]. Copyright 2013, The Electrochemical Society)

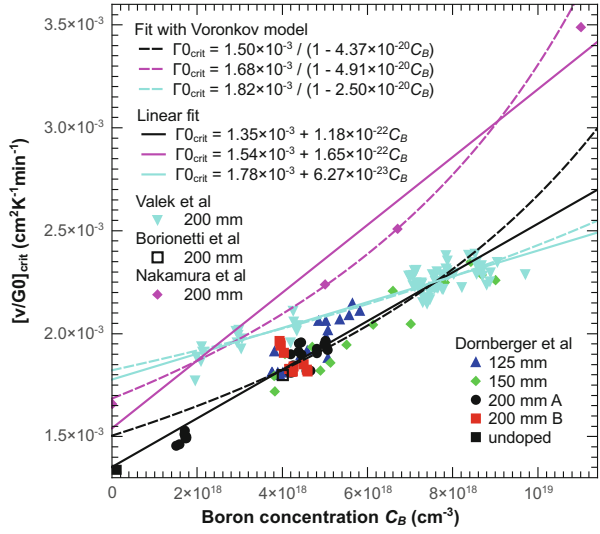


Fig. 4.47 Experimental and calculated curves obtained by taking into account dopant induced stress and Fermi level effects for a crystal grown with a thermal stress of 7.25 and 8 MPa (Reproduced with permission from [77]. Copyright 2013, The Electrochemical Society)

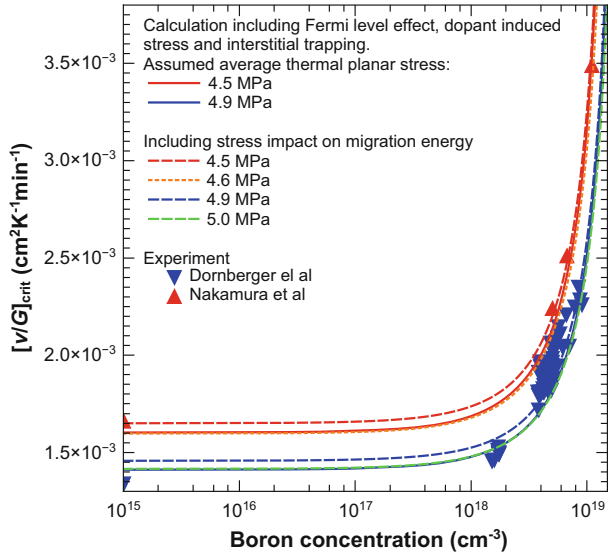
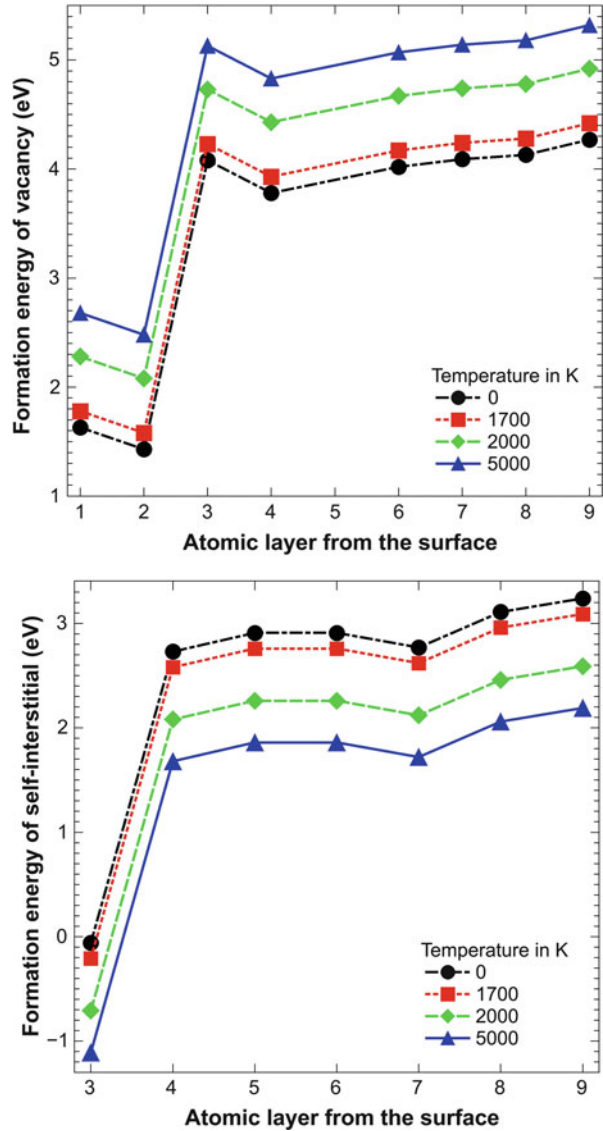


Fig. 4.48 Experimental data [15, 43] and calculated curves taking into account both dopant induced stress and Fermi level effect assuming double positively charged interstitials and neutral vacancies [77] and planar stress of 4.5 and 4.9 MPa [79]

Fig. 4.49 DFT calculations reveal a decrease of the intrinsic point defect formation energy for the vacancy (*top*) and for the interstitial (*bottom*) in the first atomic layers near the Si surface (Reprinted with permission from [26]. Copyright 2012, AIP Publishing LLC)



4.9 Conclusions and Further Work

It was shown that the impact of thermal stress, substitutional dopants and Fermi level changes, when treated separately, are well understood and can be described quantitatively. The challenges for the near future are to:

- develop a unified model taking all effects into account simultaneously;

- clarify the thermal equilibrium intrinsic point defect concentrations at the crystal-melt interface;
- clarify the mechanisms behind the experimentally observed impact of interstitial oxygen, nitrogen and hydrogen doping using ab initio calculations.

These results will be very useful in the further development of economically viable pulling processes for 450 mm, defect-free Si single-crystals and even to improve those used at the moment for the production of 300 mm crystals.

Exploring the impact of doping on the intrinsic point defect properties in Ge will also allow to clarify if it will be possible to use a similar Voronkov criterion to pull defect-free Ge crystals.

References

1. Abe, T.: The formation mechanism of grown-in defects in CZ silicon crystals based on thermal gradients measured by thermocouples near growth interfaces. *Mater. Sci. Eng. B* **73**, 16 (2000)
2. Abe, T.: Generation and annihilation of point defects by doping impurities during FZ silicon crystal growth. *J. Cryst. Growth* **334**, 4 (2011)
3. Abe, T., Takahashi, T.: Point defects in silicon melt growth from the experimental results. *ECS Trans.* **335**(11), 75 (2010)
4. Abe, T., Takahashi, T.: Intrinsic point defect behavior in silicon crystals during growth from the melt: a model derived from experimental results. *J. Cryst. Growth* **334**, 16 (2011)
5. Abe, T., Harada, H., Chikawa, J.: Swirl defects in float-zoned silicon crystals. *Physica B* **116**, 139 (1983)
6. Abe, T., Harada, H., Chikawa, J.: Microdefects and impurities in dislocation-free silicon crystals. *Mat. Res. Soc. Proc.* **14**, 1 (1983)
7. Asayama, E., Ono, T., Takeshita, M., Hourai, M., Sano, M., Tsuya, H.: Radial distribution of thermally-induced defects in heavily boron-doped silicon wafers. *Electrochem. Soc. Proc.* **98-1**, 546 (1998)
8. Bender, H., Vanhellemont, J., Schmolke, R.: High resolution structure imaging of octahedral void defects in as-grown Czochralski silicon. *Jpn. J. Appl. Phys.* **36**, L1217 (1997)
9. Dash, W.C.: Growth of silicon crystals free from dislocations. *J. Appl. Phys.* **30**, 459 (1959)
10. De Gryse, O., Clauws, P., Van Landuyt, J., Lebedev, O., Claeys, C., Simoen, E., Vanhellemont, J.: Oxide phase determination in silicon using infrared spectroscopy and transmission electron microscopy techniques. *J. Appl. Phys.* **91**, 2493 (2002)
11. de Kock, A.J.R., Stacy, W.T., van de Wijgert, W.M.: The effect of doping on microdefect formation in as-grown dislocation-free Czochralski silicon crystals. *Appl. Phys. Lett.* **34**, 611 (1979)
12. de Kock, A.J.R., van de Wijgert, W.M.: The effect of doping on the formation of swirl defects in dislocation-free Czochralski-grown silicon crystals. *J. Cryst. Growth* **49**, 718 (1980)
13. Depuydt, B., De Jonghe, M., De Baets, W., Romandic, I., Theuwis, A., Quaeys, C., Deguet, C., Akatsu, T., Letertre, F.: Germanium materials. In: Claeys, C., Simoen, E. (eds.) *Germanium-Based Technologies. From Materials to Devices*. Elsevier (2007). ISBN-13:978-0-08-044953-1
14. Dornberger, E., von Ammon, W.: The dependence of ring-like distributed stacking faults on the axial temperature gradient of growing Czochralski silicon crystals. *J. Electrochem. Soc.* **143**, 1648 (1996)

15. Dornberger, E., Gräf, D., Suhren, M., Lambert, U., Wagner, P., Dupret, F., von Ammon, W.: Influence of boron concentration on the oxidation-induced stacking fault ring in Czochralski silicon crystals. *J. Cryst. Growth* **180**, 343 (1997)
16. Dornberger, E., von Ammon, W., Virbulis, J., Hanna, B., Sinno, T.: Modeling of transient point defect dynamics in Czochralski silicon crystals. *J. Cryst. Growth* **230**, 291 (2001)
17. Dupret, F., Van den Bogaert, N., Assaker, R., Regnier, V.: Mathematical modeling of the growth of large diameter Czochralski silicon crystals considering melt dynamics. *Electrochem. Soc. Proc.* **98-1**, 396 (1998)
18. Ebe, T.: Factors determining the saturation of point defects in growing silicon crystals. *J. Crystal Growth* **203**, 387 (1999)
19. Föll, H.: http://www.tf.uni-kiel.de/matwis/amat/semi_en/index.html
20. Gräf, D., Suhren, M., Lambert, U., Schmolke, R., Ehlert, A., Ammon, W.v., Wagner, P.: Characterization of crystal quality by delineation of COP and the impact on the silicon wafer surface. *Electrochem. Soc. Proc.* **96-13**, 117 (1996)
21. Harada, K., Tanaka, H., Watanabe, T., Furuya, H.: Defects in the oxidation-induced stacking fault ring region in Czochralski silicon crystal. *Jpn. J. Appl. Phys.* **37**, 3194 (1998)
22. Hens, S., Vanhellemont, J., Poelman, D., Clauws, P., Romandic, I., Theuwis, A., Holsteyns, F., Van Steenberghe, J.: Experimental and theoretical evidence for vacancy-clustering-induced large voids in Czochralski-grown germanium crystals. *Appl. Phys. Lett.* **87**, 061915 (2005)
23. Hourai, M., Kajita, E., Nagashima, T., Fujiwara, H., Ueno, S., Sadamitsu, S., Miki, S., Shigematsu, T.: Growth parameters determining the type of grown-in defects in Czochralski silicon crystals. *Mater. Sci. Forum* **196**, 1713 (1995)
24. Hourai, M., Kelly, G.P., Tanaka, T., Umeno, S., Ogushi, S.: Control of grown-in defects in Czochralski silicon crystals. *Electrochem. Soc. Proc.* **99-1**, 372 (1999)
25. Ikematsu, Y., Mizutani, T., Nakai, K., Fujinami, M., Hasebe, M., Ohashi, W.: Transmission electron microscope observation of grown-in defects detected by bright-field infrared-laser interferometer in Czochralski silicon crystals. *Jpn. J. Appl. Phys.* **37**, L196 (1998)
26. Kamiyama, E., Sueoka, K., Vanhellemont, J.: Ab initio study of vacancy and self-interstitial properties near single crystal silicon surfaces. *J. Appl. Phys.* **111**, 083507 (2012)
27. Kamiyama, E., Vanhellemont, J., Sueoka, K., Araki, K., Izunome, K.: Thermal stress induced void formation during 450mm defect free silicon crystal growth and implications for wafer inspection. *Appl. Phys. Lett.* **102**, 082108 (2013)
28. Kissinger, G., Vanhellemont, J., Gräf, D., Claeys, C., Richter, H.: IR-LST a powerful non-invasive tool to observe crystal defects in as-grown silicon, after device processing, and in heteroepitaxial layers. *Inst. Phys. Conf. Ser.* **149**, 19 (1996)
29. Kulkarni, M.S.: Lateral incorporation of vacancies in Czochralski silicon crystals. *J. Cryst. Growth* **310**, 3183 (2008)
30. Larsen, T.L., Jensen, L., Lüdige, A., Riemann, H., Lemke, H.: Numerical simulation of point defect transport in floating-zone silicon single crystal growth. *J. Crystal Growth* **230**, 300 (2001)
31. Lee, S.H., Song, D.W., Oh, H.J., Kim, D.H.: Modeling of defects generation in 300 mm silicon monocrystals during Czochralski growth. *Jpn. J. Appl. Phys.* **49**, 121303 (2010)
32. Lemke, H., Südkamp, W.: Analytical approximations for the distributions of intrinsic point defects in grown silicon crystals. *Phys. Status Solidi A* **176**, 843 (1999)
33. Lu, Z., Kimbel, S.: Growth of 450 mm diameter semiconductor grade silicon crystals. *J. Cryst. Growth* **318**, 193 (2011)
34. Menzel, R.: Growth Conditions for Large Diameter FZ Si Single Crystals. PhD Thesis, Technical University Berlin (2013)
35. Miyazaki, M., Miyazaki, S., Yanase, Y., Ochiai, T., Shigematsu, T.: Microstructure observation of “crystal-originated particles” on silicon wafers. *Jpn. J. Appl. Phys.* **34**, 6303 (1995)
36. Miyazaki, M., Miyazaki, S., Kitamura, T., Yanase, Y., Ochiai, T., Tsuya, H.: Influence of crystal-originated “particle” microstructure on silicon wafers on gate oxide integrity. *Jpn. J. Appl. Phys.* **36**, 6187 (1997)

37. Nakamura, K.: Control of point defects in growing single crystal Si. In: Proceedings of the 7th Forum on the Science and Technology of Silicon Materials, 19–22 Oct 2014, Hamamatsu, p. 237 (2014)
38. Nakamura, K., Saishoji, T., Tomioka, J.: Simulation of point defect distributions in silicon crystals during melt-growth. *J. Cryst. Growth* **210**, 49 (2000)
39. Nakamura, K., Saishoji, T., Tomioka, J.: Grown-in defects in silicon crystals. *J. Cryst. Growth* **237–239**, 1678 (2002)
40. Nakamura, K., Maeda, S., Togawa, S., Saishoji, T., Tomioka, J.: Effect of the shape of crystal-melt interface on point defect reaction in silicon crystals. *Electrochem. Soc. Proc.* **2000–17**, 31 (2000)
41. Nakamura, K., Saishoji, T., Togawa, S., Tomioka, J.: Influence of nitrogen on the point defect reaction in silicon crystal. In: Proceedings of Forum on the Science and Technology of Silicon Materials 2001, Japan, 26–28 Nov 2001, p. 109
42. Nakamura, K., Saishoji, T., Tomioka, J.: Simulation of the point defect diffusion and growth condition for defect free Cz silicon crystal. *Electrochem. Soc. Proc.* **2002–2**, 554 (2002)
43. Nakamura, K., Suewaka, R., Saishoji, T., Tomioka, J.: The effect of impurities on the grown-in defects in Cz-Si crystals, (B, C, N, O, Sb, As, P). In: Kaneta, H.Y., Sumino, K. (eds.) Proceedings of the Forum on the Science and Technology of Silicon Materials 2003, Shonan village center, Kanagawa, 25–27 Nov 2003, p. 161
44. Nakamura, K., Suewaka, R., Ko, B.-G.: Experimental study of the impact of stress on the point defect incorporation during silicon growth. *ECS Solid State Lett.* **3**, N5 (2014)
45. Nicolai, J., Burle, N., Pichaud, B.: Determination of silicon oxide precipitate stoichiometry using global and local techniques. *J. Cryst. Growth* **363**, 93 (2013)
46. Nishimoto, M., Nakamura, K., Hourai, M., Ono, T., Sugimura, W., Motooka, T.: Determination of physical properties for point defects during Cz silicon crystal growth by high-precision thermal simulations. *J. Jpn. Inst. Met. Mater.* **75**, 657 (2011, in Japanese)
47. Raskin, G., Romandic, I., Wouters, L., Hellin, D., Teerlinck, I., Meuris, M., Mijlemans, P.: Germanium Substrates for Micro-electronic Applications up to 300mm Diameter. Presented at Symposium B: High-Mobility Group-IV Materials and Devices, of the 2004 MRS Spring Meeting, San Francisco, 12–16 Apr 2004
48. Sadamitsu, S., Umeno, S., Koike, Y., Hourai, M., Sumita, S., Shigematsu, T.: Dependence of the grown-in defect distribution on growth rates in Czochralski silicon. *Jpn. J. Appl. Phys.* **32**, 3675 (1993)
49. Schmolke, R., Angelberger, W., von Ammon, W., Bender, H.: Characterization of interstitial-related bulk defects in p^+ silicon substrates by epitaxial deposition. *Solid State Phenom.* **82–84**, 231 (2002)
50. Shiraishi, Y., Maeda, S., Nakamura, K.: Prediction of solid-liquid interface shape during CZ Si crystal growth using experimental and global simulation. *J. Cryst. Growth* **266**, 28 (2004)
51. Sinno, T.: A bottom-up multiscale view of point-defect aggregation in silicon. *J. Cryst. Growth* **303**, 5 (2007)
52. Sinno, T., Brown, R.A.: Modeling microdefect formation in Czochralski silicon. *J. Electrochem. Soc.* **146**, 2300 (1999)
53. Sinno, T., Brown, R.A., Ammon, W.v., Dornberger, E.: Point defect dynamics and the oxidation-induced stacking-fault ring in Czochralskigrown silicon crystals. *J. Electrochem. Soc.* **145**, 302 (1998)
54. Sueoka, K., Akatsuka, M., Yonemura, M., Ono, T., Asayama, E., Katahama, H.: Effect of heavy boron doping on oxygen precipitation in Czochralski silicon substrates of epitaxial wafers. *J. Electrochem. Soc.* **147**, 756 (2000)
55. Sueoka, K., Kamiyama, E., Vanhellemont, J.: Density functional theory study on the impact of heavy doping on Si intrinsic point defect properties and implications for single crystal growth from a melt. *J. Appl. Phys.* **114**, 153510 (2013)
56. Sueoka, K., Kamiyama, E., Vanhellemont, J., Nakamura, K.: Impact of plane thermal stress near the melt/solid interface on the v/G criterion for defect-free large diameter single crystal Si growth. *ECS Solid State Lett.* **3**, P69 (2014)

57. Sugimura, W., Ono, T., Umeno, S., Hourai, M., Sueoka, K.: Defect formation behaviors in heavily doped Czochralski silicon. *ECS Trans.* **2**, 95 (2006)
58. Takada, K., Yamagishi, H., Imai, M.: Research and development of super silicon wafers. *Electrochem. Soc. Proc.* **98-1**, p. 376 (1998)
59. Tan, T.Y.: Mass transport equations unifying descriptions of isothermal diffusion, thermomigration, segregation, and position-dependent diffusivity. *Appl. Phys. Lett.* **73**, 2678 (1998)
60. Tanahashi, K., Kikuchi, M., Higashino, T., Inoue, N., Mizokawa, Y.: Concentration of point defects changed by thermal stress in growing CZ silicon crystal: effect of the growth rate. *J. Cryst. Growth* **210**, 45 (2000)
61. Tracy, C.J., Fejes, P., Theodore, N.D., Maniar, P., Johnson, E., Lamm, A.J., Paler, A.M., Malik, I.J., Ong, P.: Germanium-on-insulator substrates by wafer bonding. *J. Electron. Mat.* **33**, 886 (2004)
62. Trauwaert, M.-A., Vanhellemont, J., Lambert, U., Gräf, D., Kenis, K., Mertens, P.W., Heyns, M.: Differential interference contrast microscopy of defects in as-grown and annealed Si wafers. *Solid State Phenom.* **57-58**, 387 (1997)
63. Valek, L., Lysacek, D., Sik, J.: OISF pattern and grown-in precipitates in heavily boron doped silicon. *J. Electrochem. Soc.* **154**, H904 (2007)
64. Vanhellemont, J., Claeys, C.: A theoretical study on the critical radius of precipitates and its application to silicon oxide in silicon. *J. Appl. Phys.* **62**, 3960 (1987)
65. Vanhellemont, J.: Diffusion limited oxygen precipitation in silicon: Precipitate growth kinetics and phase formation. *J. Appl. Phys.* **78**, 4297 (1995)
66. Vanhellemont, J.: Intrinsic point defect incorporation in silicon single crystals grown from a melt, revisited. *J. Appl. Phys.* **110**, 063519 (2011); Erratum: "Intrinsic point defect incorporation in silicon single crystals grown from a melt, revisited. *J. Appl. Phys.* **110**, 063519 (2011)". *J. Appl. Phys.* **110**, 129903 (2011); Response to "Comment on 'Intrinsic point defect incorporation in silicon single crystals grown from a melt, revisited'". *J. Appl. Phys.* **111**, 116102 (2012)". *J. Appl. Phys.* **111**, 116103 (2012)
67. Vanhellemont, J., Claeys, C.: A theoretical study of the critical radius of precipitates and its application to silicon oxide in silicon. *J. Appl. Phys.* **62**, 3960 (1987)
68. Vanhellemont, J., Dornberger, E., Graef, D., Esfandyari, J., Lambert, U., Schmolke, R., Ammon, W.v., Wagner, P.: Defects in as-grown Czochralski silicon: measurement, modeling and simulation. *Proceedings of the Kazusa Akademia Park Forum on the Science and Technology of Silicon Materials*, Chiba, pp. 173-196 (1997)
69. Vanhellemont, J., Senkader, S., Kissinger, G., Higgs, V., Trauwaert, M.-A., Gräf, D., Lambert, U., Wagner, P.: Measurement, modelling and simulation of defects in as-grown Czochralski silicon. *J. Cryst. Growth* **180**, 353 (1997)
70. Vanhellemont, J., De Gryse, O., Clauws, P.: Critical precipitate size revisited and implications for oxygen precipitation in silicon. *Appl. Phys. Lett.* **86**, 221903 (2005)
71. Vanhellemont, J., Simoen, E., Romandic, I., Theuws, A.: Grown-in defects in germanium. In: Claeys, C., Simoen, E. (eds.) *Germanium-Based Technologies. From Materials to Devices*, pp. 41-66. Elsevier (2007). ISBN-13:978-0-08-044953-1
72. Vanhellemont, J., Śpiwak, P., Sueoka, K., Romandic, I., Simoen, E.: Intrinsic point defect properties and engineering in silicon and germanium Czochralski crystal growth. In: *Proceedings of the 5th International Symposium on Advanced Science and Technology of Silicon Materials (JSPS Si Symposium)*, Kona, 10-14 Nov 2008 (2008). <https://www.riam.kyushu-u.ac.jp/nano/hawaii2008/>
73. Vanhellemont, J., Śpiwak, P., Sueoka, K., Simoen, E., Romandic, I.: A comparison of intrinsic point defect properties in Si and Ge. *Mater. Res. Soc. Symp. Proc.* **1070**, 1070-E06-05 (2008)
74. Vanhellemont, J., Van Steenberghe, J., Holsteys, F., Roussel, P., Meuris, M., Młynarczyk, K., Śpiwak, P., Geens, W., Romandic, I.: On the characterisation of grown-in defects in Czochralski-grown Si and Ge. *J. Mater. Sci.: Mater. Electron.* **19**, S42 (2008)
75. Vanhellemont, J., Śpiwak, P., Sueoka, K., Romandic, I.: On intrinsic point defect cluster formation during Czochralski crystal growth. *Phys. Status Solidi C* **6**, 1906 (2009)

76. Vanhellemont, J., Zhang, X., Xu, W., Chen, J., Ma, X., Yang, D.: On the assumed impact of germanium doping on void formation in Czochralskigrown silicon. *J. Appl. Phys.* **108**, 123501 (2010)
77. Vanhellemont, J., Kamiyama, E., Sueoka, K.: Silicon single crystal growth from a melt: On the impact of dopants on the v/G criterion. *ECS J. Solid State Sci. Technol.* **2**, P166 (2013)
78. Vanhellemont, J., Kamiyama, E., Sueoka, K.: Experimental study of the impact of stress on the point defect incorporation during silicon growth. *ECS Solid State Lett.* **3**, N5 (2014). *ECS Solid State Lett.* **3**, X3 (2014)
79. Vanhellemont, J., Kamiyama, E., Nakamura, K., Sueoka, K.: Intrinsic point defect behavior close to silicon melt/solid interface. In: *Proceedings of CSTIC 2015*. doi:10.1109/CSTIC.2015.7153491
80. von Ammon, W.: FZ and CZ crystal growth: cost driving factors and new perspectives. *Phys. Status Solidi A* **211**, 2461 (2014)
81. von Ammon, W., Dornberger, E., Oelkrug, H., Weidner, H.: The dependence of bulk defects on the axial temperature gradient of silicon crystals during Czochralski growth. *J. Cryst. Growth* **151**, 273 (1995)
82. Voronkov, V.V.: The mechanism of swirl defects formation in silicon. *J. Cryst. Growth* **59**, 625 (1982)
83. Voronkov, V.V., Falster, R.: Vacancy-type microdefect formation in Czochralski silicon. *J. Cryst. Growth* **194**, 76 (1998)
84. Voronkov, V.V., Falster, R.: Vacancy and self-interstitial concentration incorporated into growing silicon crystals. *J. Appl. Phys.* **86**, 5975 (1999)
85. Voronkov, V.V., Falster, R.: Grown-in microdefects, residual vacancies and oxygen precipitation bands in Czochralski silicon. *J. Cryst. Growth* **204**, 462 (1999)
86. Watanabe, M., Kramer, S.: 450 mm silicon: an opportunity and wafer scaling. *Electrochem. Soc. Interface* **15**(4), 28 (2006)
87. Wünscher, M., Lüdge, A., Riemann, H.: Crucible-free pulling of germanium crystals. *J. Cryst. Growth* **318**, 1039 (2011)
88. Yamagishi, H., Fusegawa, I., Fujimaki, N., Katayama, M.: Recognition of d-defects in silicon single-crystals by preferential etching and effect on gate oxide integrity. *Semicond. Sci. Technol.* **7**, A135 (1992)
89. Zhang, X., Xu, W., Chen, J., Ma, X., Yang, D., Gong, L., Tian, D., Vanhellemont, J.: On the impact of heavy doping on grown-in defects in Czochralski-grown silicon. *ECS Trans.* **34**(1), 1151 (2011)
90. Zhang, X., Ma, X., Yang, D., Vanhellemont, J.: Scanning infrared microscopy study of thermal processing induced defects in low resistivity Si wafers. *Semicond. Sci. Technol.* **28**, 085013 (2013)
91. Zulehner, W.: Historical overview of silicon crystal pulling development. *Mater. Sci. Eng.* **B73**, 7 (2000)